Monthly Notices of the ROYAL ASTRONOMICAL SOCIETY

MNRAS **522,** 6326–6353 (2023) https://doi.org/10.1093/mnras/stad1299
Advance Access publication 2023 April 29

MaNGA DynPop – I. Quality-assessed stellar dynamical modelling from integral-field spectroscopy of 10K nearby galaxies: a catalogue of masses, mass-to-light ratios, density profiles, and dark matter

Kai Zhu [1,2,3★] Shengdong Lu [4★] Michele Cappellari [5] Ran Li [1,2,3★] Shude Mao [4,1] and Liang Gao [1,2,3,6]

[1]*National Astronomical Observatories, Chinese Academy of Sciences, 20A Datun Road, Chaoyang District, Beijing 100101, China*
[2]*Institute for Frontiers in Astronomy and Astrophysics, Beijing Normal University, Beijing 102206, China*
[3]*School of Astronomy and Space Science, University of Chinese Academy of Sciences, Beijing 100049, China*
[4]*Department of Astronomy, Tsinghua University, Beijing 100084, China*
[5]*Sub-department of Astrophysics, Department of Physics, University of Oxford, Denys Wilkinson Building, Keble Road, Oxford OX1 3RH, UK*
[6]*Institute for Computational Cosmology, Department of Physics, University of Durham, South Road, Durham DH1 3LE, UK*

Accepted 2023 April 18. Received 2023 April 18; in original form 2022 December 11

ABSTRACT

This is the first paper in our series on the combined analysis of the Dynamics and stellar Population (DynPop) for the MaNGA survey in the final SDSS Data Release 17 (DR17). Here, we present a catalogue of dynamically determined quantities for over 10 000 nearby galaxies based on integral-field stellar kinematics from the MaNGA survey. The dynamical properties are extracted using the axisymmetric Jeans Anisotropic Modelling (JAM) method, which was previously shown to be the most accurate for this kind of study. We assess systematic uncertainties using eight dynamical models with different assumptions. We use two orientations of the velocity ellipsoid: either cylindrically aligned JAM_{cyl} or spherically aligned JAM_{sph}. We also make four assumptions for the models' dark versus luminous matter distributions: (1) mass-follows-light, (2) free NFW dark halo, (3) cosmologically constrained NFW halo, (4) generalized NFW dark halo, i.e. with free inner slope. In this catalogue, we provide the quantities related to the mass distributions (e.g. the density slopes and enclosed mass within a sphere of a given radius for total mass, stellar mass, and dark matter mass components). We also provide the complete models which can be used to compute the full luminous and mass distribution of each galaxy. Additionally, we visually assess the qualities of the models to help with model selections. We estimate the observed scatter in the measured quantities which decreases as expected with improvements in quality. For the best data quality, we find a remarkable consistency of measured quantities between different models, highlighting the robustness of the results.

Key words: galaxies: evolution – galaxies: formation – galaxies: kinematics and dynamics – galaxies: structure.

1 INTRODUCTION

In the current Lambda cold dark matter cosmological paradigm, the mass budget in the Universe is dominated by dark matter (DM) existing in the form of DM haloes. At the centre of the dark haloes, the baryonic matter condenses and forms stars, giving birth to the galaxies we observe (White & Rees 1978; White & Frenk 1991). The distributions of baryonic and DM play a crucial role in shaping the galaxies and thus are important for understanding galaxy formation and evolution mechanisms. However, due to the invisibility of DM, the observed galactic quantities are derived almost exclusively from observations of the baryonic matter, including gas and stars. A common approach to constrain the mass distribution of DM is based on the gravitational effect of DM on the motions of luminous tracers, i.e. stellar kinematics.

Since the many early studies revealing the existence of DM (e.g. Zwicky 1933, 1937, 2009; Oort 1940; Rubin & Ford 1970; Bosma & van der Kruit 1979; Rubin, Ford & Thonnard 1980; Bosma 1981; Rubin et al. 1982, 1985; Rubin, Whitmore & Ford 1988), galaxy rotation curves have been heavily used to probe the gravitational potential within which galaxies reside, and further constrain the mass distributions of galaxies. The rotation curve is usually derived from long-slit spectroscopy and only provides one-dimensional (1D) information on stellar kinematics. With the advent of Integral Field Unit (IFU) galaxy surveys, e.g. SAURON (de Zeeuw et al. 2002), ATLAS^{3D} (Cappellari et al. 2011), CALIFA (Sánchez et al. 2012), SAMI (Bryant et al. 2015), MaNGA (Bundy et al. 2015), large samples of galaxies with spatially resolved stellar kinematics are observed. The two-dimensional (2D) kinematic information can be combined with dynamical modelling methods to investigate the mass distributions of galaxies, which put constraints on the formation and evolution of galaxies.

Current popular dynamical modelling methods include action-angle distribution function based methods (Binney 2010; Bovy 2014), orbit-based Schwarzschild methods (Schwarzschild 1979;

★ E-mail: kaizhu@nao.cas.cn (KZ); lushengdong93@icloud.com (SL); ranl@bao.ac.cn (RL)

Häfner et al. 2000; Gebhardt et al. 2001; Cappellari et al. 2006; van den Bosch et al. 2008; Long & Mao 2018; Zhu et al. 2018, 2020; Neureiter et al. 2021; Zhu et al. 2022), particle-based Made-to-Measure methods (Syer & Tremaine 1996; de Lorenzi et al. 2007; Long & Mao 2010; Hunt & Kawata 2014; Zhu et al. 2014) and moment-based Jeans Anisotropic Modelling (JAM) method (Cappellari 2008, 2020). Each method has its own advantage and can be applied under different conditions. The orbit-based and particle-based methods are more flexible to be applied to galaxies with triaxial shapes and give more detailed orbital information.

However, the price to pay for this flexibility is an increased degeneracy of the resulting solutions. The degeneracy can be understood from simple dimensional arguments: the MaNGA data provide us the velocity moments at every position on the sky. This is a 2D quantity, which cannot be expected to be sufficient to constrain both the three-dimensional (3D) distribution function of the stars and the 2D or 3D gravitational potential (see discussion in Cappellari 2016, section 3.4). This implies that we need to make some assumptions to try to uncover trends in the data.

The JAM models make more restrictive assumptions, but these were shown to capture remarkably well the high signal-to-noise (S/N) stellar kinematics of large samples of real galaxies (see review by Cappellari 2016). More importantly, tests of JAM using high-resolution *N*-body simulations (Lablanche et al. 2012) and cosmological hydrodynamical simulations (Li et al. 2016) have confirmed its high accuracy and negligible bias in reproducing the total mass profiles.

More recently, JAM was compared in detail against the Schwarzschild method using samples of both observed galaxies, with circular velocities from CO gas (Leung et al. 2018), and numerical simulations (Jin et al. 2019), respectively. For the comparison with CO gas circular velocities in real galaxies, considering the radial range of 0.8–1.6 R_e, where the gas kinematics is well resolved and the rotation velocities are more accurately determined, the mean ratio for 54 galaxies between the errors of the Schwarzschild and of the JAM models is $\langle \sigma_{SCH}/\sigma_{JAM} \rangle \approx 1.7$ (Leung et al. 2018, fig. 8 and table 4). Similarly, for the recovery of enclosed masses inside a sphere of radius R_e from simulations, considering all 45 model fits (Jin et al. 2019, fig. 4), the 68 per cent percentile (1σ error) of the absolute deviations between the model results and the true values is a factor of 1.6 smaller for JAM than for Schwarzschild. In both cases, for both observations and simulations, there is no evidence for systematic biases between the true and recovered values. This higher accuracy of JAM justifies our choice of using it for this study.

JAM method has been successfully applied to many studies based on IFU data. For example, Cappellari et al. (2012, 2013a, b) construct detailed mass models, consisting of stellar and DM, for 260 early-type galaxies (ETGs) from ATLAS^{3D} survey (Cappellari et al. 2011), using JAM method. Cappellari et al. (2012) study the stellar initial mass function (IMF) of galaxies by comparing the stellar mass-to-light ratios derived from JAM with those from stellar population synthesis (SPS), reporting a strong variation of stellar IMF normalization with the velocity dispersion within an effective radius σ_e for ETGs. This correlation between galaxy IMF and velocity dispersion of ETGs is then studied and confirmed in late-type galaxies (Li et al. 2017), galaxies in a denser environment (Shetty et al. 2020), and brightest cluster galaxies (BCGs; Loubser et al. 2020, 2021), indicating a universal variation of stellar initial mass functions in various galaxies. Moreover, Cappellari et al. (2013a, b), Scott et al. (2015), and Li et al. (2018a) make use of the JAM methods to study the scaling relations, such as fundamental planes (FPs), mass planes (MPs), mass–size planes, and so on. Cappellari et al. (2015) study the total mass–density slopes (γ_T) of 14 fast-rotating ETGs and report their nearly isothermal total mass profiles, consistent with the values obtained from strong gravitational lensing analysis (Auger et al. 2010). Poci, Cappellari & McDermid (2017) and Li et al. (2019) enlarge the sample to 258 ETGs from ATLAS^{3D} and ∼2000 galaxies (including ETGs and spirals) from MaNGA DR14 (Abolfathi et al. 2018), respectively, making it possible to analyse the correlations between galaxy total density slope and other galaxy properties, e.g. velocity dispersion, halo mass, stellar mass density, and so on. These studies together show the strong ability of JAM in analysing the structure and dynamics of galaxies, and the power in understanding the galaxy evolution.

With the final data release of the MaNGA project (SDSS DR17; Abdurro'uf et al. 2022), an unprecedentedly large sample (10K) of nearby galaxies with abundant information on the kinematics and stellar population properties is available. In this series of papers, we aim to build a complete library of dynamical models for these galaxies, including mass distributions (for both stellar matter and DM), DM fractions, stellar mass-to-light ratios, inclinations, and velocity asymmetry properties, using JAM with different assumptions. With these information, we will also investigate the scaling relations, galaxy mass density slopes, as well as initial mass functions of the complete MaNGA sample. Compared to previous studies (e.g. Cappellari et al. 2012, 2013a, b, 2015; Scott et al. 2015; Li et al. 2017, 2018a, 2019; Shetty et al. 2020), our sample size will be enlarged by at least a factor of five and reach 10K galaxies for the first time. The large sample span a wide range of galactic properties, e.g. stellar mass, morphology, and central velocity dispersion, making it a statistically significant sample to explore the correlations in great detail.

In this paper (Paper I), we construct detailed JAM models for these 10 000 nearby galaxies and provide their mass distributions of both stellar and DM components. The structure of this paper is as follows. In Section 2, we briefly introduce the MaNGA survey and the data used in this work. In Section 3, we describe the methods (i.e. JAM method and the mass models applied in this work) we used to derive our quantities. In Sections 4–6, we present the dynamical modelling results and investigate their robustness and systematic uncertainties. Finally, we summarize the results in Section 7. Throughout the paper, we assume a flat Universe with $\Omega_m = 0.307$ and $H_0 = 67.7\,\mathrm{km\,s^{-1}\,Mpc^{-1}}$ (Planck Collaboration XIII 2016). The quantities in our catalogue can be converted to the standard flat cosmology with $\Omega_m = 0.3$ and $H_0 = 70\,\mathrm{km\,s^{-1}\,Mpc^{-1}}$, with very good accuracy, by multiplying enclosed masses by $K = 67.7/70$, multiplying densities (in the unit of $\mathrm{M_\odot\,pc^{-3}}$) by K^{-2}, and multiplying mass-to-light ratios by $1/K$.

2 DATA

2.1 The MaNGA survey

The Sloan Digital Sky Survey-IV (SDSS-IV) Mapping Nearby Galaxies at Apache Point Observatory (MaNGA; Bundy et al. 2015) is an IFU survey which aims at obtaining spectral measurements across the face of ∼10K nearby galaxies. Using the tightly packed arrays of optical fibres that feed into the BOSS spectrographs (Smee et al. 2013; Drory et al. 2015) on the Sloan 2.5m telescope (Gunn et al. 2006) at Apache Point Observatory, MaNGA provides the spatially resolved spectra that cover a radial range out to 1.5 effective radii (R_e) for the Primary + sample (∼2/3 of total sample) and out to 2.5 R_e for the secondary sample (∼1/3 of total sample) at higher redshift (Law et al. 2015; Wake et al. 2017). The spaxel size of MaNGA

is 0.5 arcsec and the average *g*-band point spread function (PSF) full width at half-maximum (FWHM) throughout the survey is about 2.54 arcsec (Law et al. 2016).

The spectra provided by MaNGA span a wavelength range of 3600–10 300 Å at a spectral resolution of $\sigma = 72\,\mathrm{km\,s^{-1}}$ (Law et al. 2016). Raw observational data are spectrophotometrically calibrated (Yan et al. 2016) and processed by the data reduction pipeline (DRP; Law et al. 2016) to produce 3D data cubes.

2.2 Stellar kinematics and imaging

Higher-level products such as stellar kinematics, nebular emission-line properties, and spectral indices of the galaxies are produced by the data analysis pipeline (DAP; Belfiore et al. 2019; Westfall et al. 2019). DAP derives the kinematic information from the IFU spectra of galaxies by fitting absorption lines using the PPXF software (Cappellari & Emsellem 2004; Cappellari 2017, 2022) with the combination of a subset of the MILES (Sánchez-Blázquez et al. 2006; Falcón-Barroso et al. 2011) stellar library, MILES-HC. Before fitting, the spectra are Voronoi binned (Cappellari & Copin 2003) to S/N = 10 to ensure that the derived stellar velocity dispersions are reliable. The stellar velocity dispersion presented in DAP is a combination of σ_*, the intrinsic velocity dispersion of stars, and $\sigma_{\rm diff}$, which is the quadrature difference between the instrumental dispersion of the galaxy template and the MaNGA data (Westfall et al. 2019). The velocity dispersion of the galaxy is given by $\sigma_*^2 = \sigma_{\rm obs}^2 - \sigma_{\rm diff}^2$. Note that the line spread function of MaNGA survey has been improved significantly since MPL10 (Law et al. 2021), the velocity dispersion measurements of this paper will be different from those used in Li et al. (2018a) especially for the dispersions far below instrumental resolution, which will lead to differences in dynamical modelling results.

In total, we have 10 735 DAP outputs from SDSS DR17, within which the targets of ancillary programmes (the Coma, IC342, M31, and globular clusters) should be excluded, resulting in 10 296 datacubes for galaxy observations. Among the 10 296 observations, we flag 151 datacubes that have been identified as critical-quality or unusual-quality by DRP, and the other 10 145 datacubes are high-quality observations corresponding to 10 010 unique galaxies and 135 repeat observations. We analyse 10 296 datacubes in this work since the DRP quality flag is purposely conservative (Westfall et al. 2019), but users can use the DRP quality flag (see Appendix B) to ignore the critical-quality or unusual-quality galaxies as a more conservative approach. We do not apply any other selection criteria, such that the sample enables a wide range of statistical analyses on galaxy properties as designed and can be corrected to a volume-limited sample (Wake et al. 2017). The final sample has a nearly flat stellar mass distribution in the range of $10^9 - 6 \times 10^{11}\,\mathrm{M}_\odot$ (Wake et al. 2017) and has a median redshift of $z \sim 0.03$.

In this work, we adopt the SDSS *r*-band (Stoughton et al. 2002) PSF FWHM values from the catalogue[1] provided by the MaNGA collaboration to account for the beam smearing effect on modelled stellar kinematics when comparing with the observed one (Cappellari 2008). In addition, we make use of the *r*-band images and the corresponding PSF FWHM values[2] of these ∼10 000 MaNGA galaxies from the SDSS data release 12 (Alam et al. 2015) to obtain their surface brightness.

[1] https://www.sdss.org/dr17/manga/manga-data/data-access/
[2] https://www.sdss.org/dr12/imaging/images/

3 METHOD

3.1 Jeans anisotropic modelling

In this section, we briefly introduce the mathematical basics of Jeans Anisotropic Modelling (JAM; Cappellari 2008, 2020). For a steady-state axisymmetric stellar system, the Jeans equations in cylindrical coordinates, (R, z, ϕ), are written as (Binney & Tremaine 1987, equation 4–29a,c):

$$\frac{\nu\overline{v_R^2} - \nu\overline{v_\phi^2}}{R} + \frac{\partial(\nu\overline{v_R^2})}{\partial R} + \frac{\partial(\nu\overline{v_R v_z})}{\partial z} = -\nu\frac{\partial\Phi}{\partial R}, \tag{1a}$$

$$\frac{\nu\overline{v_R v_z}}{R} + \frac{\partial(\nu\overline{v_z^2})}{\partial z} + \frac{\partial(\nu\overline{v_R v_z})}{\partial R} = -\nu\frac{\partial\Phi}{\partial z}, \tag{1b}$$

where Φ is the gravitational potential, ν is the number density of the tracer population from which one measures the kinematics, and the notation related to the stellar distribution function f is defined as

$$\nu\overline{v_k v_j} \equiv \int v_k v_j f \, \mathrm{d}^3\boldsymbol{v}. \tag{2}$$

This equation is quite general, as it *only* assumes axial symmetry and stead-state of the stellar system, but it has more unknowns than equations and cannot provide a unique solution.

To solve these equations, one has to make assumptions on the orientation of the velocity ellipsoid. Cappellari (2008) assumes that the velocity ellipsoid is aligned with the cylindrical coordinates ($\overline{v_R v_z} = 0$) and the velocity anisotropy in the meridional plane is constant,[3] quantified as

$$\beta_z \equiv 1 - \frac{\overline{v_z^2}}{\overline{v_R^2}} = 1 - \frac{\sigma_z^2}{\sigma_R^2} = 1 - \frac{1}{b}. \tag{3}$$

With these assumptions, equation (1) reduces to the following equations (Cappellari 2008, equations 8 and 9):

$$\frac{b\,\nu\overline{v_z^2} - \nu\overline{v_\phi^2}}{R} + \frac{\partial(b\,\nu\overline{v_z^2})}{\partial R} = -\nu\frac{\partial\Phi}{\partial R} \tag{4a}$$

$$\frac{\partial(\nu\overline{v_z^2})}{\partial z} = -\nu\frac{\partial\Phi}{\partial z}, \tag{4b}$$

which have a unique solution for $\overline{v_z^2}$ and $\overline{v_\phi^2}$ under the boundary condition $\nu\overline{v_z^2} = 0$ as $z \to \infty$.

The other extreme assumption to solve the Jeans equations is made by Cappellari (2020), where the velocity ellipsoid is set to be aligned with the spherical polar coordinate system (r, θ, ϕ) and the velocity anisotropy is defined as

$$\beta_r \equiv 1 - \frac{\overline{v_\theta^2}}{\overline{v_r^2}} = 1 - \frac{\sigma_\theta^2}{\sigma_r^2}. \tag{5}$$

Under these assumptions, rewriting equation (1) in spherical coordinates and assuming a spherically aligned velocity ellipsoid, the Jeans equations reduce to the following equations (Cappellari 2020, equation 7)

$$\frac{\partial(\nu\overline{v_r^2})}{\partial r} + \frac{(1+\beta_r)\,\nu\overline{v_r^2} - \nu\overline{v_\phi^2}}{r} = -\nu\frac{\partial\Phi}{\partial r} \tag{6a}$$

$$(1-\beta_r)\frac{\partial(\nu\overline{v_r^2})}{\partial\theta} + \frac{(1-\beta_r)\,\nu\overline{v_r^2} - \nu\overline{v_\phi^2}}{\tan\theta} = -\nu\frac{\partial\Phi}{\partial\theta}, \tag{6b}$$

[3] As will become clear later, the anisotropy is generally assumed constant for every component of the Multi-Gaussian Expansion, but does not have to be spatially constant for the whole galaxy.

which have a unique solution for $\overline{v_r^2}$ and $\overline{v_\phi^2}$ under the boundary condition $\nu\overline{v_r^2} = 0$ as $r \to \infty$.

For a given gravitational potential Φ, tracer density distribution ν, and velocity anisotropy (β_z or β_r), the intrinsic second velocity moments can be obtained by solving equation (4) or equation (6). The projected second velocity moments, $\overline{v_{\rm los}^2}$, can be then derived by integrating the intrinsic second velocity moments along the line-of-sight direction. By comparing the calculated line-of-sight second velocity moments and the observed root-mean-square velocity, $V_{\rm rms}$ ($\equiv \sqrt{V^2 + \sigma^2}$, where V and σ correspond to the stellar velocity and stellar velocity dispersion), we are able to constrain the model parameters (i.e. gravitational potential, velocity anisotropy, etc.). We refer the readers to Cappellari (2008, 2020) for more details of the JAM method, which is a formalism to efficiently solve equations (4) and (6) using the Multi-Gaussian Expansion (MGE; Emsellem, Monnet & Bacon 1994; Cappellari 2002) as parametrization for both the tracer population and the total density. As mentioned by Cappellari (2020), different velocity ellipsoid assumptions may be appropriate for different types of galaxies. In this work, we adopt both assumptions to construct JAM models for the complete MaNGA sample such that the readers can check the robustness of derived quantities using the consistency of the two methods. We name the JAM method with cylindrically aligned velocity ellipsoid as $\rm JAM_{cyl}$ and the one with spherically aligned velocity ellipsoid as $\rm JAM_{sph}$.

In practice, we calculate the predicted line-of-sight second velocity moments using the PYTHON version of JAM JAMPY.[4] The input total mass distribution Φ and tracer density ν of JAMPY will be parametrized with MGE models. We assume a spatially constant velocity anisotropy to simplify the models, although JAMPY allows for spatial variation of anisotropy by assigning different anisotropy values to the Gaussians of the input MGE model.

3.2 Multi-Gaussian expansion

To obtain the tracer density distribution ν, we perform Multi-Gaussian expansion (MGE; Emsellem et al. 1994; Cappellari 2002) fitting to the SDSS *r*-band images of the galaxies. The MGE formalism of surface brightness can be written as

$$\Sigma\left(x', y'\right) = \sum_{k=1}^{N} \frac{L_k}{2\pi\sigma_k^2 q_k'} \exp\left[-\frac{1}{2\sigma_k^2}\left(x'^2 + \frac{y'^2}{q_k'^2}\right)\right], \tag{7}$$

where L_k, σ_k, and q_k' are the total luminosity, dispersion along the major axis, and the axial ratio of *k*th Gaussian component. To obtain the intrinsic luminosity density distribution from the deprojection of surface brightness, the galaxies are assumed to be oblate axisymmetric following Monnet, Bacon & Emsellem (1992). Then, the 2D MGE can be deprojected to 3D space and the formalism in cylindrical coordinates can be written as (Cappellari 2008, equation 13):

$$\nu(R, z) = \sum_{k=1}^{N} \frac{L_k}{\left(\sqrt{2\pi}\sigma_k\right)^3 q_k} \exp\left[-\frac{1}{2\sigma_k^2}\left(R^2 + \frac{z^2}{q_k^2}\right)\right], \tag{8}$$

where L_k and σ_k remain the same as the 2D MGE, while q_k is the 3D intrinsic axial ratio of the *k*th Gaussian component, written as

$$q_k = \frac{\sqrt{q_k'^2 - \cos^2 i}}{\sin i}. \tag{9}$$

If we define the desired minimum intrinsic axial ratio of our deprojected MGE as $q_{\rm min} = \min(q_k)$, we can calculate the inclination ($i = 90^\circ$ being edge-on) of the MGE by inverting the previous equation as

$$\tan^2 i = \frac{1 - q_{\rm min}'^2}{q_{\rm min}'^2 - q_{\rm min}^2}, \tag{10}$$

where $q'_{\rm min} = \min(q'_k)$ is the minimum axial ratio of the projected 2D Gaussian components.

Some of the galaxies in our sample are weakly triaxial or prolate. However, the triaxial galaxies are generally close to spherical in their central parts (Emsellem et al. 2011; Cappellari 2016) and are expected to be well approximated by nearly spherical $\rm JAM_{sph}$ models. Prolate galaxies are extremely rare (Krajnović et al. 2018; Li et al. 2018b) and unlikely to play any significant role in our trends.

In this work, we make use of the PYTHON package MGEFIT[5] that implements the method by Cappellari (2002) to do the MGE fitting. Before fitting, we first go through the images of the galaxies visually and mask the foreground stars or galaxies if necessary. Then, the galaxy centre and the ellipticity are derived by the FIND_GALAXY routine in the package. We note here that the position angles (PA) used in the MGE fitting are normally the photometric ones (i.e. derived from the galaxy *r*-band image). However, we find that many of the MaNGA galaxies have different kinematic PA (calculated from their line-of-sight velocity map) and photometric PA, although the PA discrepancies of most galaxies are small. The reason for these differences is generally due to bars (e.g. Krajnović et al. 2011). As JAM assumes an axisymmetric shape, the modelled velocity field is aligned with the modelled photometry in the MGE formalism. In the presence of bars, the stellar kinematics gives a better estimate for the position angle of the underlying stellar disk than the photometry. Thus, in this work, we use the kinematic PA derived by PAFIT[6] package, which implements the method by Krajnović et al. (2006, appendix C), in the MGE fitting process, except for those galaxies with highly disturbed velocity field (visually checked). We show in Fig. 1 the comparison of JAM results based on the photometric PA and kinematic PA for the misaligned galaxy. As can be seen, for such a kinematic-photometric misaligned galaxy, a kinematic PA-based MGE results in a better root-mean-square velocity ($V_{\rm rms}$) recovery. We also confirm visually that the kinematic position angle also helps to avoid the bars or other non-axisymmetric features in the automated procedure of MGE fitting and reflects the underlying mass distribution of the whole galaxy.

Moreover, we make use of the MGE_FIT_SECTORS_REGULARIZED routine instead of MGE_FIT_SECTORS to fit the MGE formalism of galaxy photometry. This implements the method of Scott et al. (2013, section 3.2.1) to reduce the influence of bars on the model results. MGE_FIT_SECTORS_REGULARIZED here provides a narrower range of axial ratios for different Gaussian components of MGE. The MGEs so fitted artificially remove the flattest components while keeping the fitting solution only slightly changed (within the agreement of measurement uncertainties). In Fig. 2, we show several example MGE models for different kinds of galaxies (e.g. normal galaxies, kinematic-photometric misaligned galaxies, barred galaxies, and prolate galaxies).

Before performing JAM, the MGE surface brightness is multiplied by a factor of $(1 + z)^3$, with z the galaxy redshift, to account for both the bolometric cosmological dimming effect and the change of bandwidth in the AB magnitude system. Considering that most

[4]Verison 6.3.3, available from https://pypi.org/project/jampy/.

[5]Version 5.0.13, from https://pypi.org/project/mgefit/.

[6]Version 2.0.7, from https://pypi.org/project/pafit/.

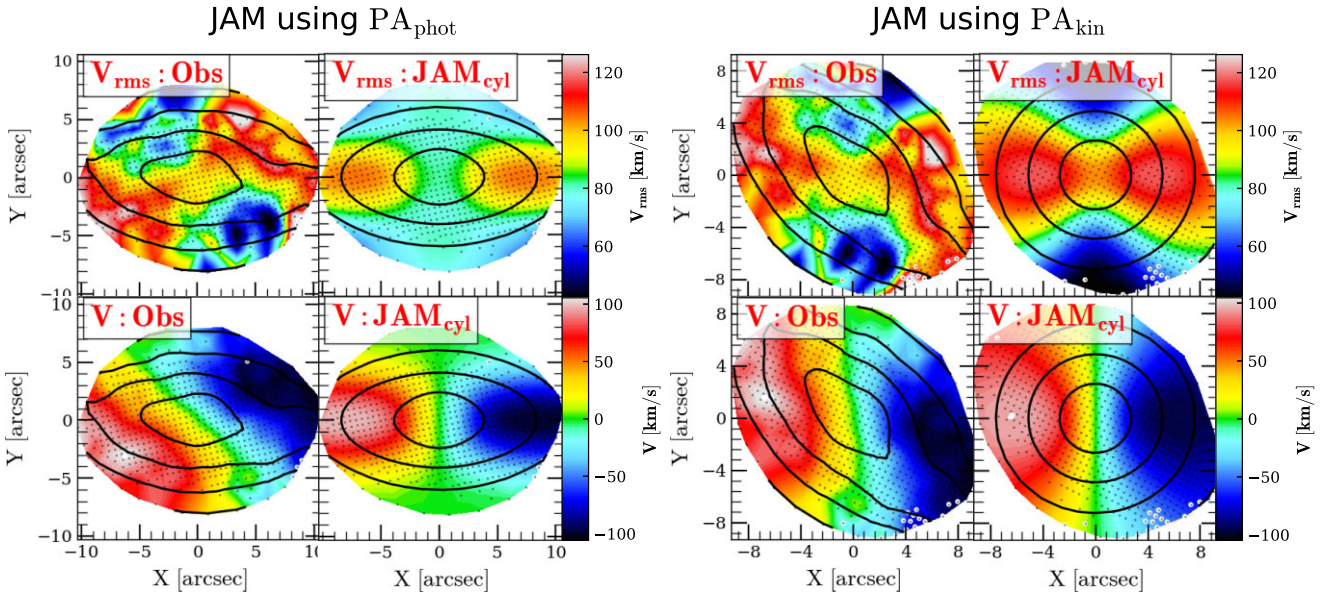

Figure 1. An example of the comparison between aligning models with the photometric or kinematic position angles (PA) for a barred galaxy (MaNGA ID: 1–155463). The left subfigure is the fitting result of $\mathrm{JAM_{cyl}}$ + MFL model (see Section 3 for definition) by assuming the galaxy major axis is aligned with the bar, which here defines the photometric PA. The right subfigure shows the model results by aligning the JAM model with the kinematic PA. In each subfigure, the observed second velocity moment $V_{\rm rms}$ and the light-of-sight velocity V are shown in the left-hand panels, and the corresponding modelled maps are in the right-hand panels. All the kinematic maps are oriented in the way that the major (photometric or kinematic) axis is oriented along the x-direction. The black contours are the observed (left-hand panels) and modelled (right-hand panels) surface brightness contours in steps of 1 mag, respectively. The black dots are the centroids of the Voronoi bins from which the maps were linearly interpolated.

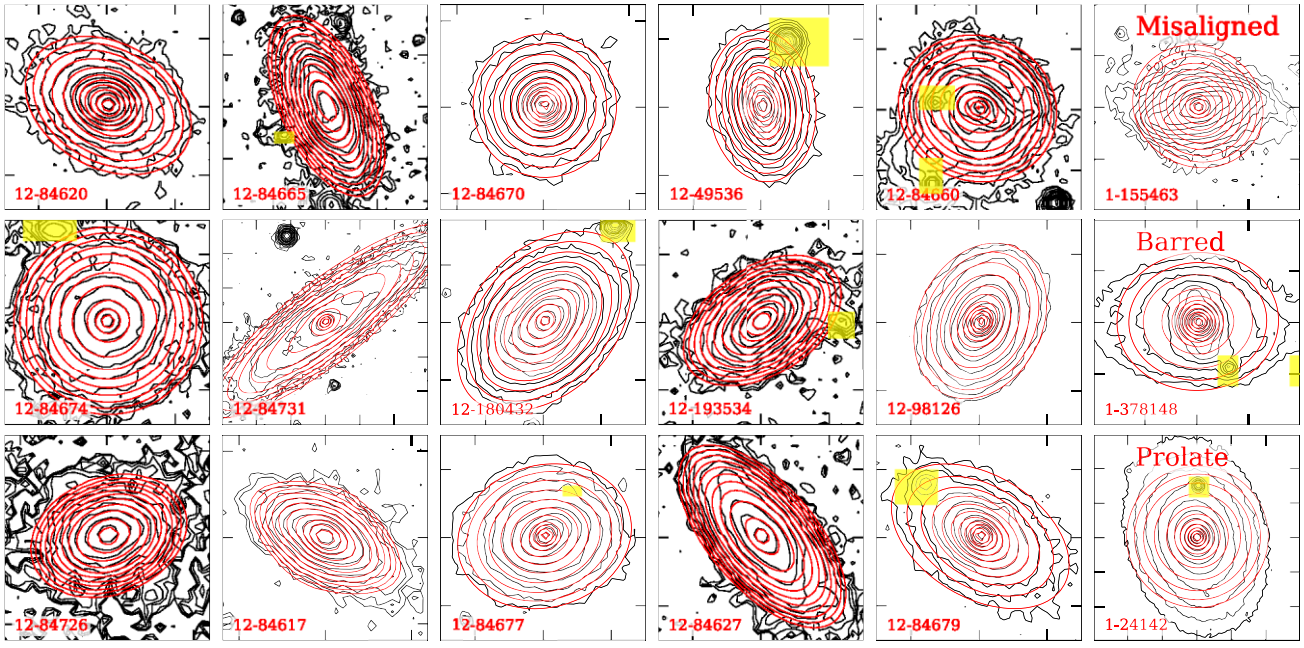

Figure 2. SDSS r-band photometry of example galaxies (black curves) with MGE model contours (red curves) overplotted. MaNGA ID is presented in each panel. The first five columns: randomly selected galaxies with similar photometric position angles and kinematic position angles. The rightmost column shows a photometric-kinematic misaligned galaxy, a galaxy with a strong bar, and a prolate galaxy from top to bottom. In each panel, the yellow shaded regions are the masked regions, which are excluded in MGE fitting. Each tick in all panels is 10 arcsec. In all the fittings, the kinematic position angle is used (see Section 3.2).

of the MaNGA galaxies locate at low redshift, we do not apply K-correction (Hogg et al. 2002). Throughout this work, we adopt the r-band absolute solar magnitude as $\mathrm{M_{\odot,r}} = 4.65$ in AB system (Willmer 2018).

3.3 Mass models and parameter design

The gravitational potential, Φ, is determined by the total mass distribution, consisting of an extended matter distribution (stellar

matter and DM) and a supermassive black hole at the centre of the galaxy. The mass of black hole is estimated using the $M_{BH} - \sigma_c$ relation (McConnell et al. 2011), where σ_c is computed as mean stellar velocity dispersion within an aperture of radius equal to the FWHM of the MaNGA PSF. Below, we describe the mass models adopted in this work.

3.3.1 Model A: mass-follows-light JAM model

Mass-follows-light model (MFL, hereafter) is also known as the self-consistent model (e.g. Cappellari et al. 2013a; Shetty et al. 2020). In this model, we assume that both the distribution of the kinematic tracer population ν and the total mass of the galaxy follows the *r*-band luminosity distribution and thus can be obtained from the luminosity MGEs by multiplying a constant dynamical mass-to-light ratio, *M*/*L*. Therefore, there are three free parameters that are needed to fit in order to match the observed V_{rms}: (1) the velocity dispersion ratio σ_z/σ_R in JAM_{cyl} (or σ_θ/σ_r in JAM_{sph}), (2) the minimum intrinsic axial ratio q_{min} which we use to parametrize the inclination, and (3) the dynamical mass-to-light ratio *M*/*L*.

3.3.2 Model B: JAM model with NFW dark halo

This model allows for the decomposition between the stellar mass distribution and DM mass distribution. In this case, the kinematic tracer population ν is still deprojected from the observed stellar surface brightness. However, the mass distribution has extra freedom. It is described as a superposition of the deprojected stellar luminosity, scaled by a spatially constant stellar mass-to-light ratio M_*/L, plus a spherical NFW (Navarro, Frenk & White 1996) dark halo. Contrary to what is sometimes incorrectly stated, this kind of model is formally correct even in the presence of spatial *M*/*L* gradients in the galaxy. In fact, with *M*/*L* variations the tracer population ν is still best approximated by the surface brightness (not by the surface density) and the model would still return a formally correct estimate of the total density. What would be biased in this case is our interpretation of the total density decomposition in terms of luminous and dark components. The NFW profile is written as

$$\rho_{DM}(r) = \rho_s \left(\frac{r}{r_s}\right)^{-1} \left(\frac{1}{2} + \frac{1}{2}\frac{r}{r_s}\right)^{-2}, \quad (11)$$

where r_s is the characteristic radius and ρ_s is the characteristic density. To reduce the number of free parameters, we calculate the characteristic radius r_s with scaling relations, instead of setting it to be a free parameter: at each step of parameters optimization procedure, r_s is calculated by the redshift-dependent stellar-to-halo mass relation (Moster, Naab & White 2013), and the redshift-dependent mass–concentration relation (Dutton & Macciò 2014), with a given stellar mass (or stellar mass-to-light ratio). We fix the limits of the r_s to be $5 \times r_{max,bin} < r_s < 250$ kpc, with $r_{max,bin}$ the largest radius of the Voronoi bins, to avoid unrealistic small/large r_s. The lower limit of $5 \times r_{max,bin}$ is approximately the median value of the $r_{s,NSA}$ distribution, which are estimated using the Chabrier-IMF stellar mass and the scaling relations described above. The upper limit of 250 kpc is large enough to ensure that the halo profiles with $r_s > 250$ kpc are nearly identical (at least within the kinematic data range of MaNGA) to the one with $r_s = 250$ kpc. The choice of r_s is not a critical assumption: the characteristic radius of halo is much larger (at a median ratio of 5) than the kinematic data range of MaNGA, indicating that the halo profile within observed region of MaNGA can be described as a simple power-law density profile. Therefore, this model has four free parameters: (1) the minimum intrinsic axial ratio q_{min}, (2) the anisotropy σ_z/σ_R or σ_θ/σ_r, (3) the stellar mass-to-light ratio M_*/L, and (4) the characteristic density of NFW halo ρ_s.

3.3.3 Model C: JAM model with fixed NFW dark halo

The model is similar to Model B, but assumes an NFW dark halo profile without any free parameter. Both ρ_s and r_s are inferred from the scaling relations used in Model B, which means that the inclusion of dark halo is predicted by the simulations. Thus, there are only three free parameters of this model: (1) q_{min}, (2) σ_z/σ_R in JAM_{cyl} (or σ_θ/σ_r in JAM_{sph}), and (3) M_*/L.

3.3.4 Model D: JAM model with gNFW dark halo

We also adopt a more general dark halo profile, the generalized NFW (gNFW, Wyithe, Turner & Spergel 2001) profile, in this work to allow for the baryonic effect on the inner density slope of dark halo (Abadi et al. 2010; Duffy et al. 2010; Laporte et al. 2012). The only difference between this model and Model B is the inner mass density slope within the characteristic radius of the dark halo. The gNFW profile can be written as

$$\rho_{DM}(r) = \rho_s \left(\frac{r}{r_s}\right)^{\gamma} \left(\frac{1}{2} + \frac{1}{2}\frac{r}{r_s}\right)^{-\gamma-3}, \quad (12)$$

where $\gamma = -1$ results in an NFW profile, similar to Model B. The variation of γ allows for more kinds of dark halos, including some special cases such as the ones with an inner core ($\gamma \approx 0$). We estimate the characteristic radius r_s here the same as Model B, and thus there are five free parameters in this model: (1) q_{min}, (2) σ_z/σ_R in JAM_{cyl} (or σ_θ/σ_r in JAM_{sph}), (3) M_*/L, (4) ρ_s, and (5) γ.

For simplicity, we name the four JAM models (A–D) following their assumptions on the dark halos, i.e. MFL model = Model A, NFW model = Model B, fixed NFW model = Model C, and gNFW model = Model D.

3.3.5 Parameter limits

We note here that, with given r_s and γ (being -1 for an NFW dark halo), the characteristic density ρ_s can be uniquely calculated from the stellar mass-to-light ratio and the DM fraction within a given aperture. Thus, we take the DM fraction within a sphere with its radius being the 2D projected half-light radius R_e, f_{DM} ($<R_e$) as the free parameter in NFW and gNFW models, instead of ρ_s. In this way, we do not need to worry about the boundary of ρ_s, but simply set the range $0 < f_{DM}(<R_e) < 1$. The 2D effective radius R_e here is computed using MGE_HALF_LIGHT_ISOPHOTE software in JAMPY package and then multiplied by 1.35 as described in Section 4.1.

In addition, the boundary of velocity anisotropy parameter is important for recovering the galaxy inclination (or equivalently the minimum intrinsic axial ratio q_{min}). In previous studies with JAM_{cyl}, the boundary of β_z was constrained to be $\beta_z > 0$ (equivalently, $\sigma_z/\sigma_R < 1$) to break the inclination-anisotropy degeneracy (Cappellari 2008). A similar criterion cannot be applied to the JAM_{sph} models and for this reason we explore if we can place limits on σ_θ/σ_r, to ensure that the JAM_{sph} inferred inclination is consistent with the inclination determined from the geometry of dust discs in galaxies. For the MaNGA galaxies, we visually select 12 galaxies with dust rings. The dust rings are assumed to be circular and thus the observed ellipticity of the ring is thought to be only from the effect of the inclination. We fit ellipses to the extracted dust ring to obtain the

upper and lower limit of the axial ratio and then calculate the range of galaxy inclination. More details about the procedure can be found in Appendix A. In Fig. 3, we show the contours of $\Delta\chi^2$ on the (σ_z/σ_R, i), or (σ_θ/σ_r, i) plane. $\Delta\chi^2$ is defined as

$$\Delta\chi^2 \equiv \chi^2 - \chi^2_{\rm min}, \tag{13}$$

where χ^2 is the fitted residual of the MFL model (both $\rm JAM_{cyl}$ and $\rm JAM_{sph}$) with a set of given $[\sigma_z/\sigma_R, i]$ (or $[\sigma_z/\sigma_R, i]$ in $\rm JAM_{sph}$); $\chi^2_{\rm min}$ is the minimum value of all the possible χ^2. As can be seen, for $\rm JAM_{cyl}$, most of the galaxies show a strong degeneracy between σ_z/σ_R and i and only assuming $\sigma_z/\sigma_R < 1$ can the JAM inferred inclination match the one derived from the dust ring in agreement with Cappellari (2008). For $\rm JAM_{sph}$, however, the degeneracy between σ_θ/σ_r and i is weaker. Therefore, there is no need to set a strict upper limit on σ_θ/σ_r because the best-fitting model can always recover the galaxy inclination. In this work, we adopt a rather extreme upper limit $\sigma_\theta/\sigma_r < 2$ ($\beta_r > -3$) that has never been observed in real galaxies.

In the course of this project, we had to run the JAM models multiple times while trying to understand the differences between model results and optimize the reliability of our extracted parameters. We discovered cases where the $\rm JAM_{cyl}$ and $\rm JAM_{sph}$ models provided quite different total density slopes. Analysing these deviant cases, we realized this was due to the mass-anisotropy degeneracy (Binney & Mamon 1982; Gerhard 1993) allowing for unrealistic values of the anisotropy and making the $\rm JAM_{sph}$ return unreliable density profiles, due to modest quality data. Rather than simply exclude those galaxies as unreliable, we used our extensive knowledge of the anisotropy, accumulated from many detailed dynamical models of nearby galaxies, as a prior to reduce this degeneracy and extract as much useful information as we could from the data.

In particular, we now know that fast rotator galaxies satisfy an approximate upper limit in anisotropy (e.g. Cappellari 2016, fig. 9), which has recently been explained as due to a physical limit on high-anisotropy equilibrium solutions in flat galaxies (Wang, Cappellari & Peng 2021). The limit has the form (Cappellari 2016, equation 11)

$$\beta \lesssim 0.7 \times \varepsilon_{\rm intr}, \tag{14}$$

and appears valid for both cylindrical and spherical alignment of the velocity ellipsoid (Wang et al. 2021).

Rewriting equation (14), the empirical lower boundary of velocity dispersion ratio is

$$\mathcal{R}(q) = \sqrt{0.3 + 0.7q}, \qquad \sigma_z/\sigma_R \gtrsim \mathcal{R}(q), \qquad \sigma_\theta/\sigma_r \gtrsim \mathcal{R}(q), \tag{15}$$

where q is the characteristic intrinsic axial ratio of the galaxy. These limits are derived for fast rotators galaxies; however, they are also known to apply to slow rotators, which are generally close to spherical in the central parts and close to isotropic (Gerhard et al. 2001; Gebhardt et al. 2003; Cappellari et al. 2007; Thomas et al. 2009). In conclusion, we restrict $\mathcal{R}(q) < \sigma_z/\sigma_R < 1$ and $\mathcal{R}(q) < \sigma_\theta/\sigma_r < 2$ in this work. The parameters and their boundaries of different JAM models are summarized in Table 1.

The characteristic intrinsic axial ratio q is estimated as follows: deprojecting the observed MGE with the inclination angle derived from the initial fitting procedure using MFL models (Section 3.4.2), then re-projecting the intrinsic MGE with $i = 90^\circ$ and obtaining the ellipticity of the re-projected MGE, $\varepsilon_{\rm intr}$, from the MGE_HALF_LIGHT_ISOPHOTE software in the JAMPY package, finally the intrinsic axial ratio q is calculated by $q \equiv 1 - \varepsilon_{\rm intr}$.

3.4 Parameter optimizations

3.4.1 optimization tools

We use two different tools to find the best-fitting parameters of the JAM models. The first is a least-squares fitting method. In this work, we make use of the `scipy.optimize.least_squares` routine of the PYTHON software SCIPY[7] (Virtanen et al. 2020). To avoid the possibility that the fitted parameters are stuck in a local minimum, we further adopt the `scipy.optimize.direct` global optimisation algorithm (Jones, Perttunen & Stuckman 1993), as originally implemented by Gablonsky & Kelley (2001), to find a starting guess for the least-squares optimization.

To be able to assess the degeneracies and formal uncertainties in the model parameters from the posterior distribution, as well as to be more robust against the possibility of missing the global minimum, we also employ a Bayesian inference method. According to the Bayes theorem, the posterior probability distribution of the model with a given set of parameters $\boldsymbol{p}$, given a set of data $\boldsymbol{d}$ is

$$P(\boldsymbol{p}|\boldsymbol{d}) \propto P(\boldsymbol{d}|\boldsymbol{p}) \times P(\boldsymbol{p}), \tag{16}$$

where $P(\boldsymbol{d}|\boldsymbol{p})$ is the likelihood of the data, given some model, and $P(\boldsymbol{p})$ is the prior on our model. Assuming that the observational errors are Gaussian, the likelihood $P(\boldsymbol{d}|\boldsymbol{p})$ is proportional to $\exp\left(-\frac{\chi^2}{2}\right)$, where χ^2 is defined as

$$\chi^2 = \sum_j \left[\frac{\left(\overline{v^2_{{\rm los},j}}\right)^{1/2} - V_{{\rm rms},j}}{\varepsilon_{V_{{\rm rms},j}}} \right]^2, \tag{17}$$

where $\overline{v^2_{{\rm los},j}}$ is the modelled second moment velocity of jth Voronoi bin; $V_{{\rm rms},j}$ and $\varepsilon_{V_{{\rm rms},j}}$ are the corresponding observed root-mean-square velocity and 1σ uncertainties (see Section 3.4.2 for more details on error estimation). The summation goes over all the Voronoi bins of MaNGA DAP outputs. In this work, we adopt the software PYMULTINEST[8] (Buchner et al. 2014), a PYTHON version of the efficient and robust Bayesian tool MULTINEST (Feroz, Hobson & Bridges 2009; Feroz et al. 2019), which is a multimodal nested sampling algorithm, to carry out the Bayesian inference of the model parameters. The priors needed in the Bayesian inference are set to be flat within the given boundary as shown in Table 1. The best-fitting model refers to the set of parameters that has the maximum likelihood (corresponding to maximum posterior probability in the case of flat priors). We adopt 500 active points and 0.8 sampling efficiency for PYMULTINEST in this work.

In Fig. 4, we present the comparison between the χ^2/DOF derived from the least-squares fitting and the Bayesian inference, adopting the $\rm JAM_{cyl}$ method and the gNFW mass model. As can be seen, the χ^2/DOF are highly consistent between different optimization methods for the Qual $\geqslant 1$ galaxies (see Section 5.1 for the definitions of Qual). To investigate the convergence of optimization methods for the galaxies with bad modelling quality, we randomly select 100 galaxies ($\sim$40 Qual $\leqslant 0$ galaxies) from the complete MaNGA sample and find a similar level of high convergence. In summary, we apply least-squares fitting on the complete sample for all models, but only apply the Bayesian inference on the Qual $\geqslant 1$ galaxies for the gNFW model to obtain the posterior distributions of parameters (both $\rm JAM_{cyl}$ and $\rm JAM_{sph}$).

[7] https://scipy.org

[8] Version 2.11, https://pypi.org/project/pymultinest/.

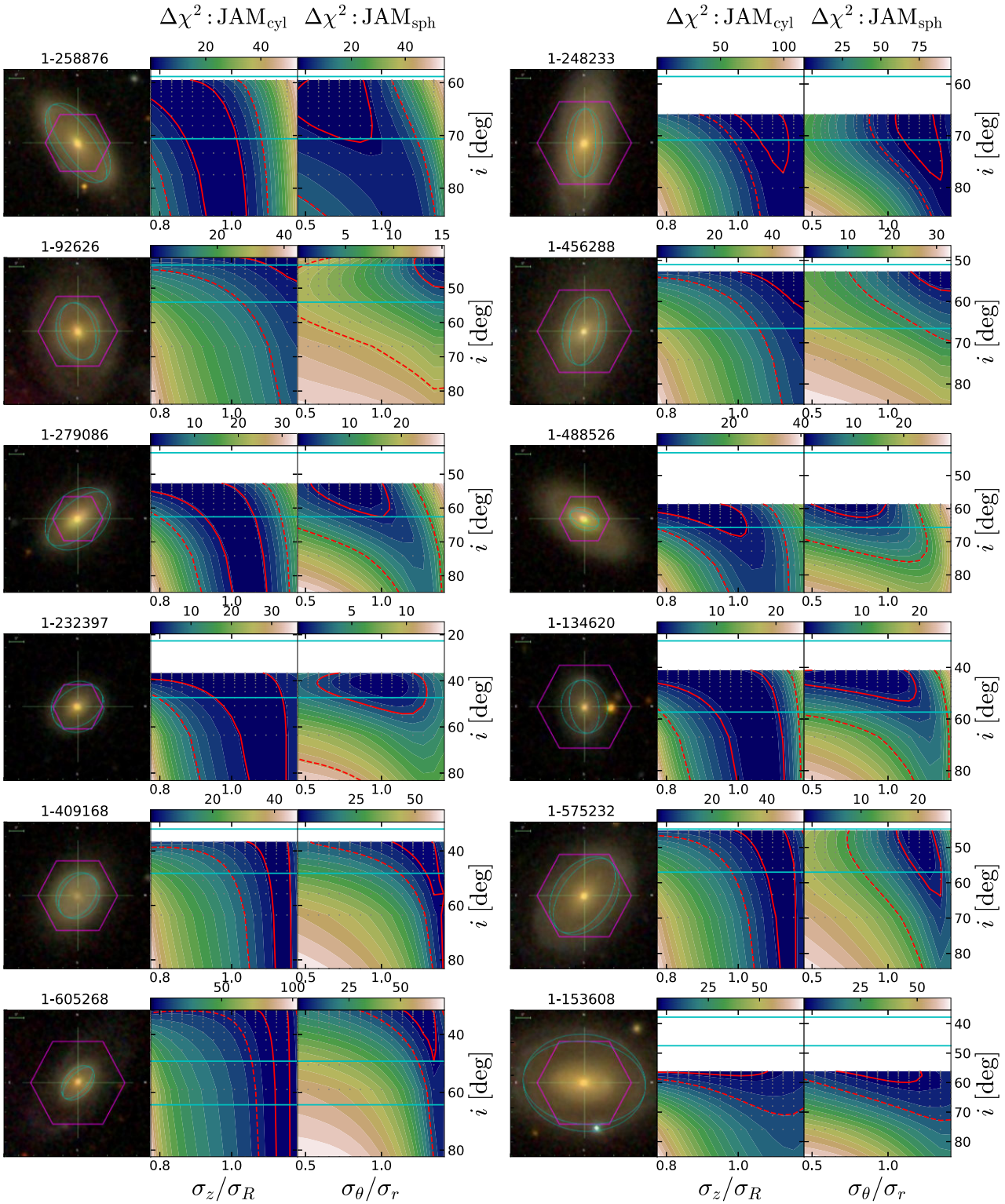

Figure 3. The $\Delta\chi^2$ ($\equiv \chi^2 - \chi^2_{\rm min}$) distributions on the inclination-velocity anisotropy planes for 12 selected galaxies with dust rings (see Section 3.3 for model design). χ^2 values are the fitted residuals of MFL models with a given inclination-velocity anisotropy parameter pair; $\chi^2_{\rm min}$ is the minimum value of all the possible χ^2. In each subfigure, the left-hand panel shows the image of the galaxy with the two ellipses indicating the upper and lower limit of apparent axial ratios. Results of JAM$_{\rm cyl}$ and JAM$_{\rm sph}$ are shown in the middle and right-hand panels of each subfigure, with the horizontal blue lines indicating the range of inclination angle determined from the dust geometry (see Section 3.3.5 for details). The red solid and dashed contours represent 1σ ($\Delta\chi^2 = 2.3$) and 3σ ($\Delta\chi^2 = 11.8$) confidence levels of the fitting. The degeneracy between the velocity anisotropy and the inclination is strong for the JAM$_{\rm cyl}$, while the degeneracy is weaker for JAM$_{\rm sph}$, requiring more(less) restrictive boundaries of velocity anisotropy for JAM$_{\rm cyl}$ (JAM$_{\rm sph}$).

Table 1. Parameter design, parameter boundary, the optimization methods for eight models (see Sections 3.1 and 3.3). $q'_{\rm min}$ is the minimum observed axial ratio, $\mathcal{R}(q)$ is the empirical lower limit of velocity dispersion ratio determined from equation (15).

Models	Free parameters					optimization method
	$q_{\rm min}$	$\sigma_z/\sigma_R(\sigma_\theta/\sigma_r)$	$\lg M/L[{\rm M}_\odot/{\rm L}_\odot]$	$f_{\rm DM}(<R_{\rm e})$	γ	
(A1) $\rm JAM_{cyl}$ + MFL	$[0.05, q'_{\rm min}]$	σ_z/σ_R: $[\mathcal{R}(q), 1]$	$\lg(M/L)_{\rm e}$: $[-2, 2]$	–	–	DIRECT + LEAST-SQUARES
(A2) $\rm JAM_{sph}$ + MFL	$[0.05, q'_{\rm min}]$	σ_θ/σ_r: $[\mathcal{R}(q), 2]$	$\lg(M/L)_{\rm e}$: $[-2, 2]$	–	–	DIRECT + LEAST-SQUARES
(B1) $\rm JAM_{cyl}$ + NFW	$[0.05, q'_{\rm min}]$	σ_z/σ_R: $[\mathcal{R}(q), 1]$	$\lg M_*/L$: $[-2, 2]$	$[0, 1]$	–	DIRECT + LEAST-SQUARES
(B2) $\rm JAM_{sph}$ + NFW	$[0.05, q'_{\rm min}]$	σ_θ/σ_r: $[\mathcal{R}(q), 2]$	$\lg M_*/L$: $[-2, 2]$	$[0, 1]$	–	DIRECT + LEAST-SQUARES
(C1) $\rm JAM_{cyl}$ + fixed NFW	$[0.05, q'_{\rm min}]$	σ_z/σ_R: $[\mathcal{R}(q), 1]$	$\lg M_*/L$: $[-2, 2]$	–	–	DIRECT + LEAST-SQUARES
(C2) $\rm JAM_{sph}$ + fixed NFW	$[0.05, q'_{\rm min}]$	σ_θ/σ_r: $[\mathcal{R}(q), 2]$	$\lg M_*/L$: $[-2, 2]$	–	–	DIRECT + LEAST-SQUARES
(D1) $\rm JAM_{cyl}$ + gNFW	$[0.05, q'_{\rm min}]$	σ_z/σ_R: $[\mathcal{R}(q), 1]$	$\lg M_*/L$: $[-2, 2]$	$[0, 1]$	$[-1.6, 0]$	Qual = 0: DIRECT + LEAST-SQUARES Qual ⩾ 1: MULTINEST
(D2) $\rm JAM_{sph}$ + gNFW	$[0.05, q'_{\rm min}]$	σ_θ/σ_r: $[\mathcal{R}(q), 2]$	$\lg M_*/L$: $[-2, 2]$	$[0, 1]$	$[-1.6, 0]$	Qual = 0: DIRECT + LEAST-SQUARES Qual ⩾ 1: MULTINEST

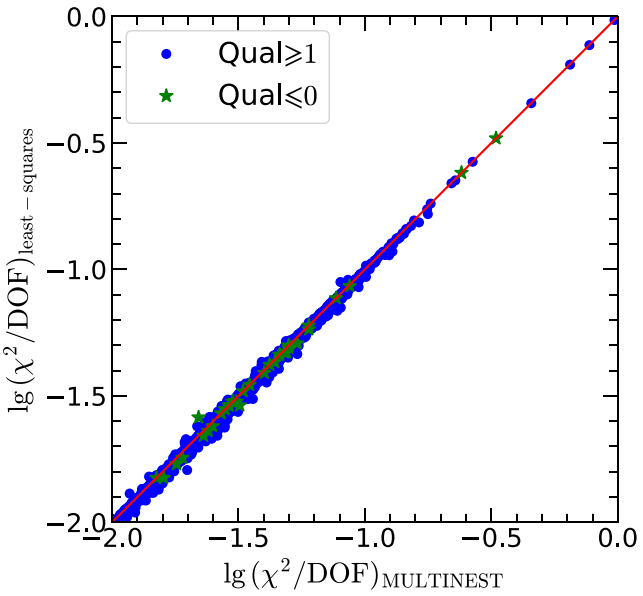

Figure 4. Comparisons of the χ^2/DOF derived from MULTINEST (X-axis) and from least-squares fitting (Y-axis). The JAM method with cylindrically aligned velocity ellipsoid (i.e. $\rm JAM_{cyl}$, see Section 3.1 for definition) is applied on the gNFW model (see Section 3.3) for 6065 Qual ⩾ 1 galaxies (blue circles). We also randomly select 100 galaxies, among which are ∼40 Qual ⩽ 0 galaxies (green stars), to investigate the convergence of optimization methods for galaxies with bad modelling quality. Qual ⩾ 1 and Qual ⩽ 0 refer to the better modelling qualities and worse modelling qualities, respectively (see the definitions in Section 5.1). The red solid line represents the $y = x$ relation.

3.4.2 *Fitting procedure*

The fitting procedure can be divided into two steps. In the first step, we perform an initial fitting with $\rm JAM_{cyl}$ on an MFL model (Table 1), which aims at removing some spurious kinematics features like stars or the problematic bins of the data and determining the kinematic errors. The first aim of this step is achieved by iteratively fitting the kinematics and clipping the bins with deviation beyond 3σ confidence of the noise, until convergence. We compute the noise as a bi-weight estimate (Hoaglin, Mosteller & Tukey 1983) from the differences of the data and model $V_{\rm rms}$. Then the remained bins will be adopted in the following processes of optimization, including either the least-squares fitting or the Bayesian inference. Two examples of the clipped kinematic maps are shown in Fig. 5.

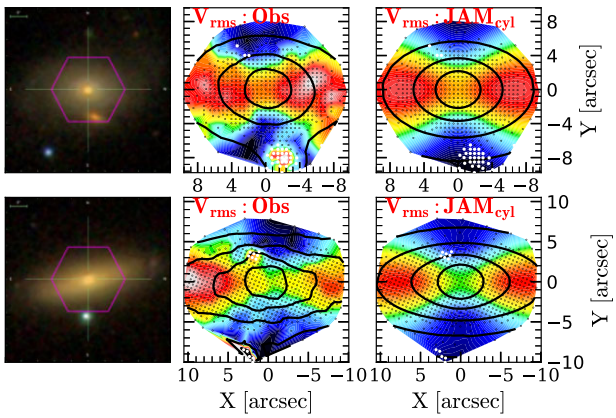

Figure 5. Examples of pixel clipping in JAM modelling. The white circles in the velocity fields are the clipped bins, corresponding to the spurious kinematics features caused by satellite galaxies or foreground stars, which are not fitted in JAM.

We also determine the kinematic errors $\varepsilon_{V_{\rm rms}}$ from the initial fitting with $\rm JAM_{cyl}$ + MFL model in the first step. In order to prevent the dynamical models from being strongly affected by the inner high-S/N Voronoi bins, we do not use the true observed kinematic errors. Instead, we follow the practice in Mitzkus, Cappellari & Walcher (2017), where the initial kinematic errors of $V_{\rm rms}$ are derived by error propagation as

$$\varepsilon^{\rm init}_{V_{\rm rms}} = \frac{1}{V_{\rm rms}}\sqrt{(V\,\varepsilon_V)^2 + (\sigma\varepsilon_\sigma)^2}, \tag{18}$$

where the errors on velocity and velocity dispersion (ε_V and ε_σ) are set to be $\varepsilon_{\rm V} = 5$ km s^{-1} and $\varepsilon_\sigma = 0.05\sigma$, respectively. After the initial fitting process with $\varepsilon^{\rm init}_{V_{\rm rms}}$, we compute the χ^2 and scale the uncertainties using

$$\varepsilon_{V_{\rm rms}} = \varepsilon^{\rm init}_{V_{\rm rms}} \times \sqrt{\chi^2/{\rm DOF}} \times (2N_{\rm bins})^{1/4}, \tag{19}$$

where χ^2/DOF is the reduced chi-square value of the initial fitting and $N_{\rm bins}$ is the number of remained kinematic bins after the initial fitting. The two scaling factors of $\sqrt{\chi^2/{\rm DOF}}$ and $(2N_{\rm bins})^{1/4}$ are used to first increase the kinematic errors to reach $\chi^2/{\rm DOF} = 1$ and second to try to account, in an approximate way, for possible systematic uncertainties (Mitzkus et al. 2017). This approach is a Bayesian implementation of the idea that was suggested for confidence levels based on χ^2 by van den Bosch & van de Ven (2009) and was since used on numerous papers based on large IFS data sets.

In the second step, the clipped kinematic maps and the renewed kinematic errors $\varepsilon_{V_{\rm rms}}$ are used in the final parameter estimation (both for the least-squares fitting and the Bayesian inference) to obtain the final results of the eight models listed in Table 1.

4 THE CATALOGUE

We create a catalogue containing the dynamical properties of MaNGA galaxies derived from JAM method. The complete list together with brief descriptions is shown in Appendix B. We clarify the calculations of some of the derived quantities below.

4.1 Size parameters

We provide three size parameters in this catalogue, namely $R_{\rm e}^{\rm maj}$, $R_{\rm e}$, and $r_{1/2}$. Here, $R_{\rm e}^{\rm maj}$ is the major axis of the half-light elliptical isophote; $R_{\rm e}$ is the circularized effective radius, satisfying that the area of half-light ellipse $A = \pi R_{\rm e}^2$, and $r_{1/2}$ is the radius of the 3D sphere which encloses half of the total luminosity of the galaxy. For spherical galaxies $r_{1/2} \approx 1.33 R_{\rm e}$ for a wide range of profiles shape (Ciotti 1991). However, for more general flattened galaxies the ratio between these two radii varies wildly with inclination and shape (Cappellari et al. 2013a, fig. 4). The projected size parameters $R_{\rm e}$ and $R_{\rm e}^{\rm maj}$ are calculated from the MGE formalism of the galaxy r-band luminosity distribution, using the MGE_HALF_LIGHT_ISOPHOTE software in JAMPY. The $r_{1/2}$ is computed by linear interpolation on the deprojected luminosity profile, which is derived for a set of given radii using the MGE_RADIAL_MASS software and adopting the best-fitting inclination for each model (thus the $r_{1/2}$ values for different models are similar but not totally the same). In Cappellari et al. (2013a), the 2D effective radii (i.e. $R_{\rm e}^{\rm maj}$ and $R_{\rm e}$), which are derived using the same photometric data (SDSS r-band imaging) and technique, are scaled by a factor of 1.35 to match the values determined from 2MASS (Skrutskie et al. 2006) plus RC3 (de Vaucouleurs et al. 1991). We adopt the same correction and all quantities related to the 2D effective radii in this catalogue always use the scaled radii.

4.2 Mass and mass density slopes

For all of the eight models (four mass models with both $\rm JAM_{cyl}$ and $\rm JAM_{sph}$), we provide total mass within given apertures and total mass slopes. For the 6 models allowing decomposition of DM and stellar mass, we also derived mass and slopes for DM and stellar component separately.

Enclosed masses (stellar matter, DM) are calculated analytically using the MGE_RADIAL_MASS routine in JAMPY, within 2 different spheres [i.e. with radii being $R_{\rm e}$ and $r_{1/2}$, respectively], denoted as $M_{\rm T}(<R_{\rm e})$ [or $M_*(<R_{\rm e})$ and $M_{\rm DM}(<R_{\rm e})$ for stellar matter and DM] and $M_{\rm T}(<r_{1/2})$ [or $M_*(<r_{1/2})$ and $M_{\rm DM}(<r_{1/2})$ for stellar matter and DM]. We also give the dynamical mass-to-light ratio $(M/L)_{\rm e}$ as the ratio between $M_{\rm T}(<R_{\rm e})$ and the r-band luminosity within a sphere of $R_{\rm e}$.[9]

We calculate two kinds of density slopes. One is the average logarithmic slope $\gamma_{\rm T}$ (Cappellari et al. 2015; Poci et al. 2017), which can be written as

$$\gamma_{\rm T} = \frac{1}{\lg(R_{\rm out}/R_{\rm in})}\int_{R_{\rm in}}^{R_{\rm out}} \frac{{\rm d}\lg\rho_{\rm T}}{{\rm d}\lg r}{\rm d}\lg r = \frac{\lg\rho_{\rm T}(R_{\rm out}) - \lg\rho_{\rm T}(R_{\rm in})}{\lg R_{\rm out} - \lg R_{\rm in}}, \tag{20}$$

[9]Note that the so-calculated dynamical mass-to-light ratio coincides with the free parameter M/L used in the MFL model.

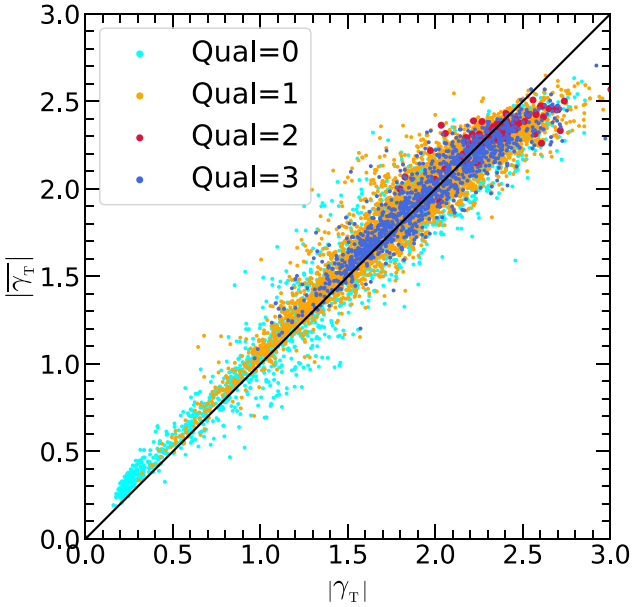

Figure 6. The comparison of the absolute values between two definitions of total density slopes: the average logarithmic slope $\gamma_{\rm T}$ (x-axis) and the mass-weighted slope $\overline{\gamma_{\rm T}}$ (y-axis). The symbols with different colours represent the galaxies with different modelling qualities (see Section 5.1 for the definitions). The black straight line is the $y = x$ relation.

where $R_{\rm out}$ is set to be $R_{\rm e}$, and $R_{\rm in}$ is set to be the maximum between $0.1R_{\rm e}$ and the FWHM of MaNGA PSF.

The other one is the mass-weighted density slope $\overline{\gamma_{\rm T}}$ (Dutton & Treu 2014), given by

$$\overline{\gamma_{\rm T}} \equiv \frac{1}{M_{\rm T}(<R_{\rm e})}\int_0^{R_{\rm e}} -\frac{{\rm d}\lg\rho_{\rm T}}{{\rm d}\lg r} 4\pi r^2 \rho_{\rm T}(r){\rm d}r = 3 - \frac{4\pi R_{\rm e}^3 \rho_{\rm T}(R_{\rm e})}{M_{\rm T}(<R_{\rm e})}. \tag{21}$$

The mass density slopes for the stellar matter (γ_*, $\overline{\gamma_*}$) and DM components ($\gamma_{\rm DM}$, $\overline{\gamma_{\rm DM}}$) can also be calculated similarly. In all cases, the radially averaged density is computed analytically from the axisymmetric MGE using the MGE_RADIAL_DENSITY function within JAMPY. We provide slopes of both definitions in the catalogue, but only show the mass-weighted slopes in the analysis in the following sections. Note that the two definitions have opposite signs: the average logarithmic slope is negative, while the mass-weighted one is positive. A comparison between the two definitions of the total density slopes (the absolute values) is presented in Fig. 6.

4.3 Effective velocity dispersion and stellar angular momentum

The effective second moments $\langle v_{\rm rms}^2\rangle_{\rm e}$ is defined as the luminosity-weighted second velocity moments within an elliptical aperture of area $A = \pi R_{\rm e}^2$, which reads:

$$\langle v_{\rm rms}^2\rangle_{\rm e} = \frac{\sum_k F_k(V_k^2 + \sigma_k^2)}{\sum_k F_k}, \tag{22}$$

where F_k, V_k, and σ_k are the flux, stellar velocity, and stellar velocity dispersion in the kth spaxel, respectively. As V and σ are derived from the PPXF fit to the Voronoi binned spectra, we replicate the binned values for each spaxel belonging to each Voronoi bin. The effective velocity dispersion $\sigma_{\rm e}$, which is measured from a single fit to the stacked spectra within half-light ellipse, is found to be close to $\langle v_{\rm rms}^2\rangle_{\rm e}$ within the random errors (Cappellari et al. 2013a). The proxy for the

Table 2. Parameter guidance for MaNGA galaxies in different quality groups (see Section 5.1 for definition of the groups). From left to right, the columns are (1) quality classification; (2) the number of galaxies; (3) the guidance for the use of quantities; (4) the reliable JAM-inferred parameters. For each quality (i.e. Qual = 0, 1, 2, 3), the reliable parameters for all galaxies in the given quality group (top) and for those galaxies satisfying the recommended selection criteria (bottom) are presented in the fourth column. Even for the reliable parameters for all galaxies (e.g. $M_{\rm T}(<R_{\rm e})$, $M_{\rm T}(<r_{1/2})$, $(M/L)_{\rm e}$, $\gamma_{\rm T}$, $\overline{\gamma_{\rm T}}$ for Qual $\geqslant 1$ galaxies), we recommend to further select the galaxies satisfying $|\lg(X_{\rm cyl}/X_{\rm sph})| < 3\Delta$ (enclosed total masses or M/L) or $|X_{\rm cyl} - X_{\rm sph}| < 3\Delta$ (total density slopes) to remove the outliers. Here, $X_{\rm cyl}$ and $X_{\rm sph}$ represent the quantities derived from $\rm JAM_{cyl}$ and $\rm JAM_{sph}$ models, respectively. The Δ is the rms scatter of each quantity in different quality groups, which is taken from Table 3. The users can use more (or less) restrictive selection criteria to obtain purer (or more complete) samples based on their scientific purpose.

Qual	$N_{\rm gal}$	Guidance	Reliable parameters
−1	936	No kinematic/dynamical properties should be used.	None
0	3295	$\sigma_{\rm e}$ and $\lambda_{R_{\rm e}}$ can be trusted. JAM-inferred parameters should be used with cautions: only the consistent $\rm JAM_{cyl}$ and $\rm JAM_{sph}$ inferred integrated quantities, i.e. the total mass within a sphere ($R_{\rm e}$ or $r_{1/2}$) or the total M/L within $R_{\rm e}$, can be used (see Section 6.2).	$\sigma_{\rm e}$, $\lambda_{R_{\rm e}}$ $M_{\rm T}(<R_{\rm e})$, $M_{\rm T}(<r_{1/2})$: $\lvert\lg(X_{\rm cyl}/X_{\rm sph})\rvert < 3\Delta$ $(M/L)_{\rm e}$: $\lvert\lg(X_{\rm cyl}/X_{\rm sph})\rvert < 3\Delta$
1	4833	$\sigma_{\rm e}$ and $\lambda_{R_{\rm e}}$ can be trusted. Parameters related to the total mass distribution (e.g. total mass within $R_{\rm e}$, total mass-to-light ratios, and total density slopes) can be trusted. Parameters related to the decomposition between stellar matter and DM components (e.g. DM fraction within $R_{\rm e}$) should be used with cautions: only consistent $\rm JAM_{cyl}$ and $\rm JAM_{sph}$ inferred values can be trusted.	$\sigma_{\rm e}$, $\lambda_{R_{\rm e}}$, $M_{\rm T}(<R_{\rm e})$, $M_{\rm T}(<r_{1/2})$, $(M/L)_{\rm e}$, $\gamma_{\rm T}$, $\overline{\gamma_{\rm T}}$ $f_{\rm DM}(<R_{\rm e})$: $\lvert X_{\rm cyl} - X_{\rm sph}\rvert < 0.1$ M_*/L: $\lvert\lg(X_{\rm cyl}/X_{\rm sph})\rvert < 0.1$
2	90	$\sigma_{\rm e}$ and $\lambda_{R_{\rm e}}$ can be trusted. Parameters related to the total mass distribution (e.g. total mass within $R_{\rm e}$, total mass-to-light ratios and total density slopes) can be trusted. Parameters related to the decomposition between stellar matter and DM components (e.g. DM fraction within $R_{\rm e}$) should be used with cautions: only consistent $\rm JAM_{cyl}$ and $\rm JAM_{sph}$ inferred values can be trusted.	$\sigma_{\rm e}$, $\lambda_{R_{\rm e}}$, $M_{\rm T}(<R_{\rm e})$, $M_{\rm T}(<r_{1/2})$, $(M/L)_{\rm e}$, $\gamma_{\rm T}$, $\overline{\gamma_{\rm T}}$ $f_{\rm DM}(<R_{\rm e})$: $\lvert X_{\rm cyl} - X_{\rm sph}\rvert < 0.1$ M_*/L: $\lvert\lg(X_{\rm cyl}/X_{\rm sph})\rvert < 0.1$
3	1142	All quantities are regarded as reliable.	All

stellar angular momentum $\lambda_{R_{\rm e}}$ is defined as (Emsellem et al. 2007)

$$\lambda_{R_{\rm e}} = \frac{\sum_k F_k R_k |V_k|}{\sum_k F_k R_k \sqrt{V_k^2 + \sigma_k^2}}, \tag{23}$$

where F_k, V_k, and σ_k are the same as equation (22); R_k is the distance of kth spaxel to the galaxy centre. We calculate these two quantities following Graham et al. (2018) as their code has been made publicly available,[10] and the values have been corrected for PSF effects.

5 QUALITY ASSESSMENT

The quality and characteristics of the data vary widely for a survey like MaNGA. For this reason, for a proper use of our catalogue, it is essential to be able to select subsets according to the quality of the models. In this section, we discuss our qualitative assessment.

5.1 Visual quality classification

The MaNGA sample contains various types of galaxies, some of which, including merging galaxies, galaxy pairs, irregular galaxies, and strong bars, cannot be described by the dynamical models which assume a steady state. In other cases, the data quality is low because of low *S*/*N* or strong dust absorptions. We thus grade the fitting quality by visually inspecting $V_{\rm rms}$ and V maps recovered with the MFL model.

We grade the modelling quality as −1, 0, 1, 2, 3 according to the following principles. Qual = −1 means the galaxies' stellar kinematics are highly disturbed (e.g. merging galaxies, irregular galaxies, or close galaxy pairs). One should not trust any of the kinematic/dynamic properties of these galaxies. Qual = 0 represents the galaxies with somewhat regular kinematic distributions but cannot be well-modelled by JAM, indicating inferior data quality (low S/N or low stellar velocity dispersion) or a problematic model (e.g. due to the presence of strong bars). Qual = 1 indicates an acceptable fit to the $V_{\rm rms}$ with the $V_{\rm rms}$ shape being somewhat predicted but the value being biased. Qual = 2 corresponds to the cases that have a good fit (both shape and value) to the $V_{\rm rms}$ but a bad fit to the line-of-sight velocity V (see Section 5.2 for the prediction of line-of-sight velocities). The highest quality Qual = 3 means that both $V_{\rm rms}$ and V are well recovered. The numbers of galaxies in each quality group and the suggestions on the parameters than can be trusted in each quality group are given in Table 2. The example kinematic maps of different modelling qualities are shown in Fig. 7.

In Fig. 8, we present the distributions of samples with different data qualities (except for Qual = −1) on the colour–magnitude diagram, the redshift-stellar mass diagram, and the redshift-apparent magnitude diagram, which are derived from the NASA-Sloan Atlas[11] (NSA) catalogue (see Blanton & Roweis 2007; Blanton et al. 2011). Moreover, we also present the $(\lambda_{R_{\rm e}}, \varepsilon)$ diagram in the bottom right-hand panel of Fig. 8. Compared to the parent sample, diverse distributions of stellar mass (or equivalently *r*-band absolute magnitude) are observed for different modelling qualities: the Qual = 0 sample contains a higher fraction of low-mass galaxies, the distributions of Qual = 1 galaxies are flat, which is similar to the whole sample, while most of the Qual = 2 sample are massive galaxies. The stellar mass of Qual = 3 galaxies span in a range of 10^{10}–$10^{11.3}$ $\rm M_\odot$. Note that the fitting quality has a strong dependence on the data quality of the spectrum. Some of the most massive ellipticals have low modelling

[10] https://github.com/marktgraham/lambdaR_e_calc

[11] http://nsatlas.org/

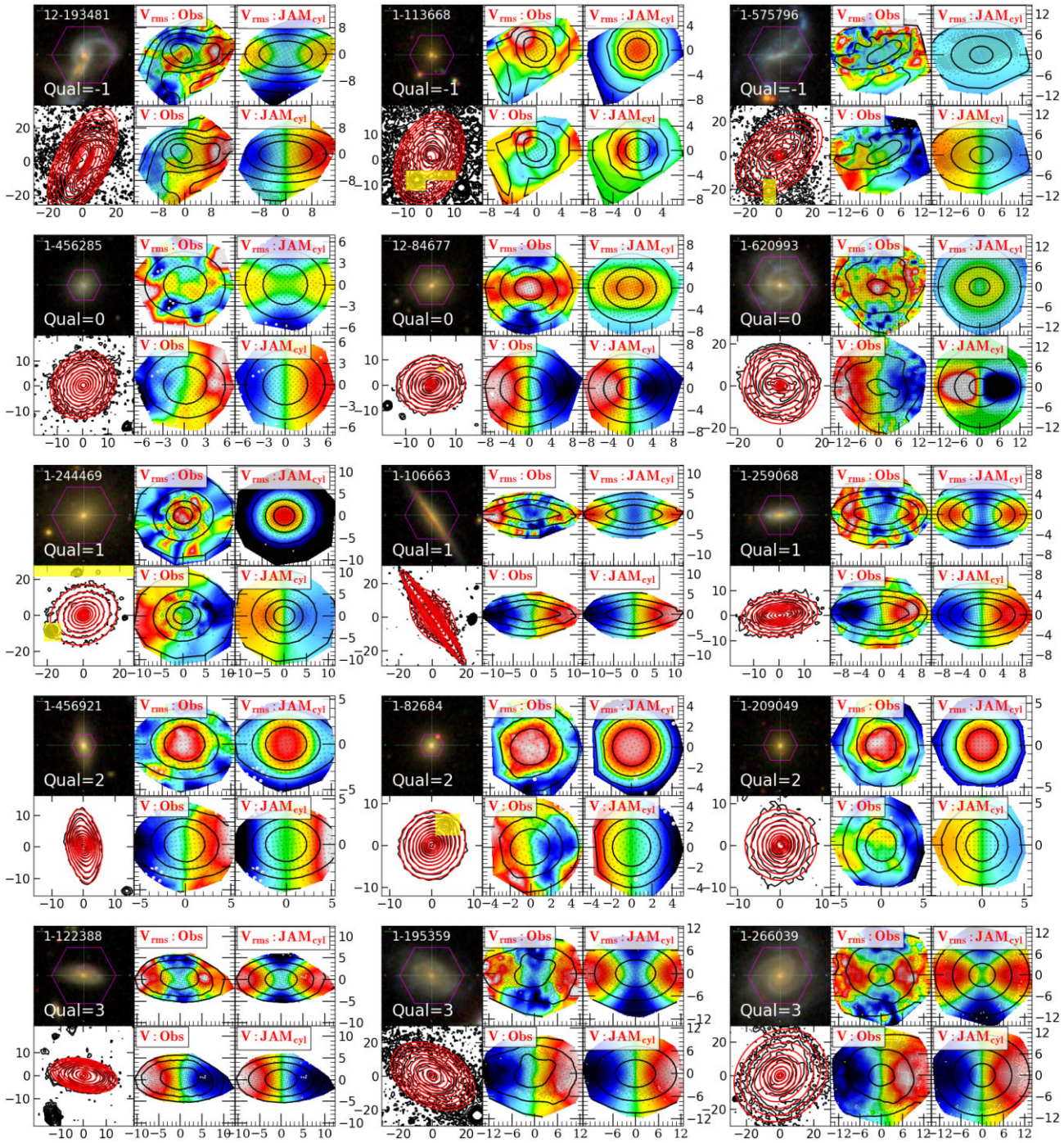

Figure 7. Examples of galaxies with different modelling qualities (from top to bottom: Qual $= -1$, 0, 1, 2, and 3). For each galaxy, the RGB image, observed and modelled stellar kinematics (both $V_{\rm rms}$ and V), and SDSS r-band isophotes (black) overlaid with MGE contours (red) are presented. The contours, lines, and symbols are the same as Figs 1 and 2.

quality because they have a low S/N spectrum (confirmed by the bottom left-hand panel of Fig. 8: the modelling quality strongly depends on the apparent magnitude). The colour distributions are nearly identical to the whole sample except for the Qual $= 2$ sample, which has a higher fraction of red galaxies. In particular, most of Qual $= 2$ galaxies are massive and red, suggesting that they could be slow rotator galaxies and we confirm this in the $(\lambda_{R_e}, \varepsilon)$ diagram. As expected, the Qual $= 3$ galaxies contain more fast rotators compared to the parent sample, while the distributions of λ_{R_e} and ε for Qual $= 0$ and Qual $= 1$ galaxies are very similar to the parent sample. We present some examples of the observed and modelled $V_{\rm rms}$ maps for the Qual $= 3$ galaxies in Fig. 9.

5.2 Predictions on the first velocity moments

The gravitational potential in a galaxy is only constrained by the even moment of the velocity. This is because, for a given density and tracer distributions and one can always revert the sense of rotation

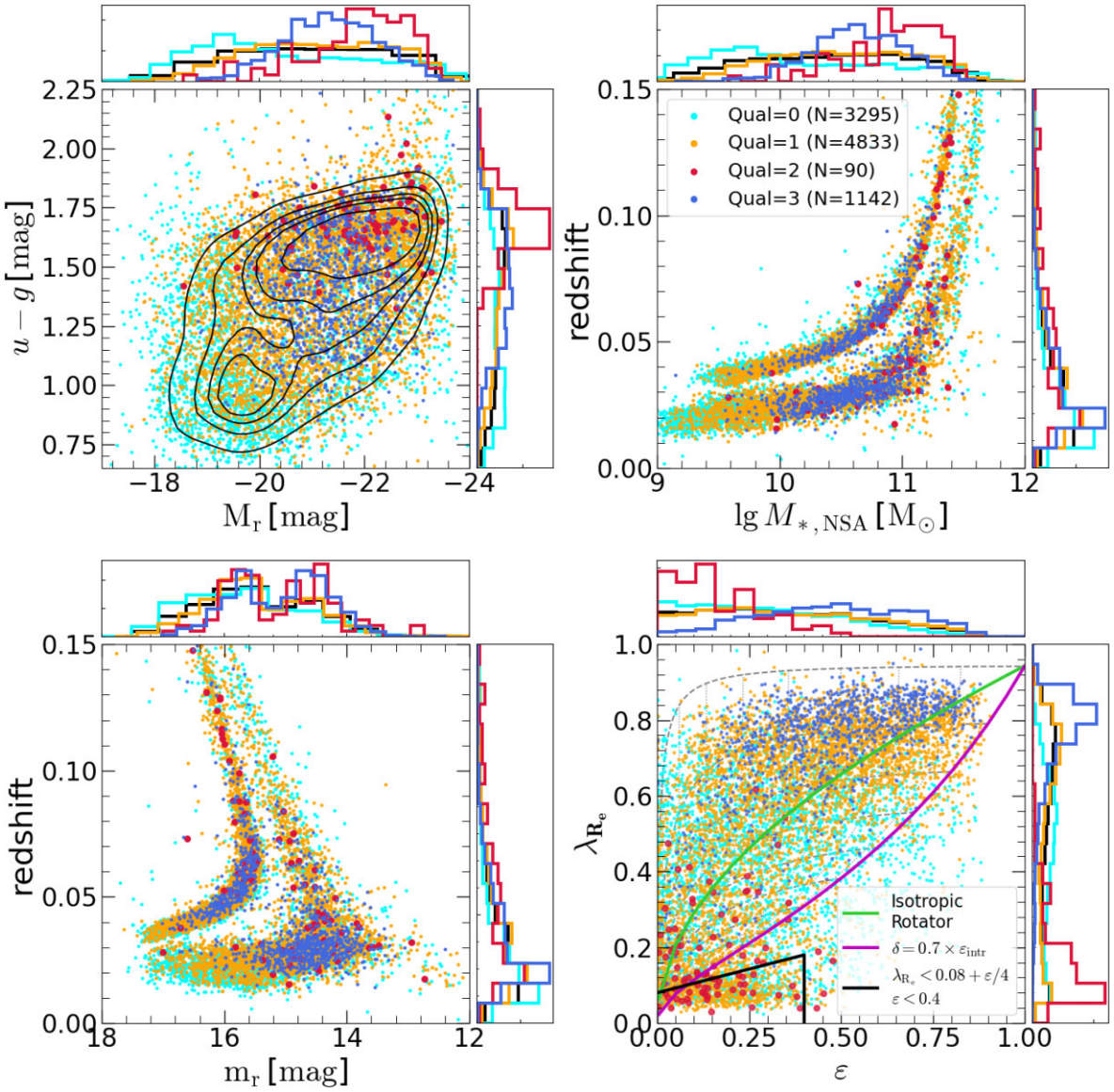

Figure 8. The distributions of MaNGA complete sample in the $u-g$ colour–magnitude (SDSS r-band) diagram (top left-hand panel), the redshift-stellar mass diagram (top right-hand panel), the redshift-apparent magnitude (SDSS r-band) diagram (bottom left-hand panel), and the (λ_{R_e}, ε) diagram (bottom right-hand panel). Galaxies with different modelling qualities are shown with different colours (see the legend). The black contours are the distribution of the total sample. Histograms of each panel show the probability density functions for the whole sample (black) and each subsample of different modelling qualities. All the parameters are extracted from the NSA catalogue except for the (λ_{R_e}, ε) diagram, where λ_{R_e} is calculated as Section 4.3 and ε is the observed ellipticity derived from the MGE models using the MGE_HALF_LIGHT_ISOPHOTE software. In the (λ_{R_e}, ϵ) diagram, the green line represents the predicted relation for an edge-on ($i = 90°$) isotropic rotator from Binney (2005) (Cappellari 2016, equation 14), while the magenta line denotes the edge-on relation from Cappellari et al. (2007) (Cappellari 2016, equation 11). The thin dotted lines show how the magenta line changes with different inclinations ($\Delta i = 10°$), while the thick dashed lines show how the galaxies move across the diagram with changing inclination for a set of given $\varepsilon_{\mathrm{intr}}$ values ($\Delta\varepsilon_{\mathrm{intr}} = 0.1$). The lower left-hand region enclosed by the black solid lines ($\lambda_{R_e} < 0.08 + \varepsilon/4$, $\varepsilon < 0.4$) define the region occupied by slow rotators (Cappellari 2016, equation 19).

(change velocity sign) of arbitrary numbers of tracer stars, without having to change neither the density nor the tracer. For this reason, in our fitting process, as customary with JAM models, we only use the second velocity moments V_{rms} to determine the free parameters that define the galaxy shape and density distribution. To predict the projected second velocity moments, we do not need to make any assumption on how the second moment in the tangential direction $\overline{v_\phi^2}$, which appears in the Jeans equations (4) and (6), separates into ordered rotation and a random motion, defined by

$$\overline{v_\phi^2} = \overline{v_\phi}^2 + \sigma_\phi^2. \tag{24}$$

To further obtain the line-of-sight velocity (i.e. the first velocity moment) map, one needs to make additional assumptions on the shape of velocity ellipsoid to evaluate $\overline{v_\phi}$. In this work, to quantify galaxy rotations we predict the velocities assuming an oblate velocity ellipsoid which satisfies

$$\sigma_\phi^2 = \sigma_R^2, \qquad \sigma_\phi^2 = \sigma_r^2, \tag{25}$$

in the cylindrically or spherically aligned cases, respectively, where σ_R^2 (σ_r^2) is determined from $\mathrm{JAM_{cyl}}$ ($\mathrm{JAM_{sph}}$) model, following Cappellari (2008, 2020). In the case of $\mathrm{JAM_{sph}}$, there are two

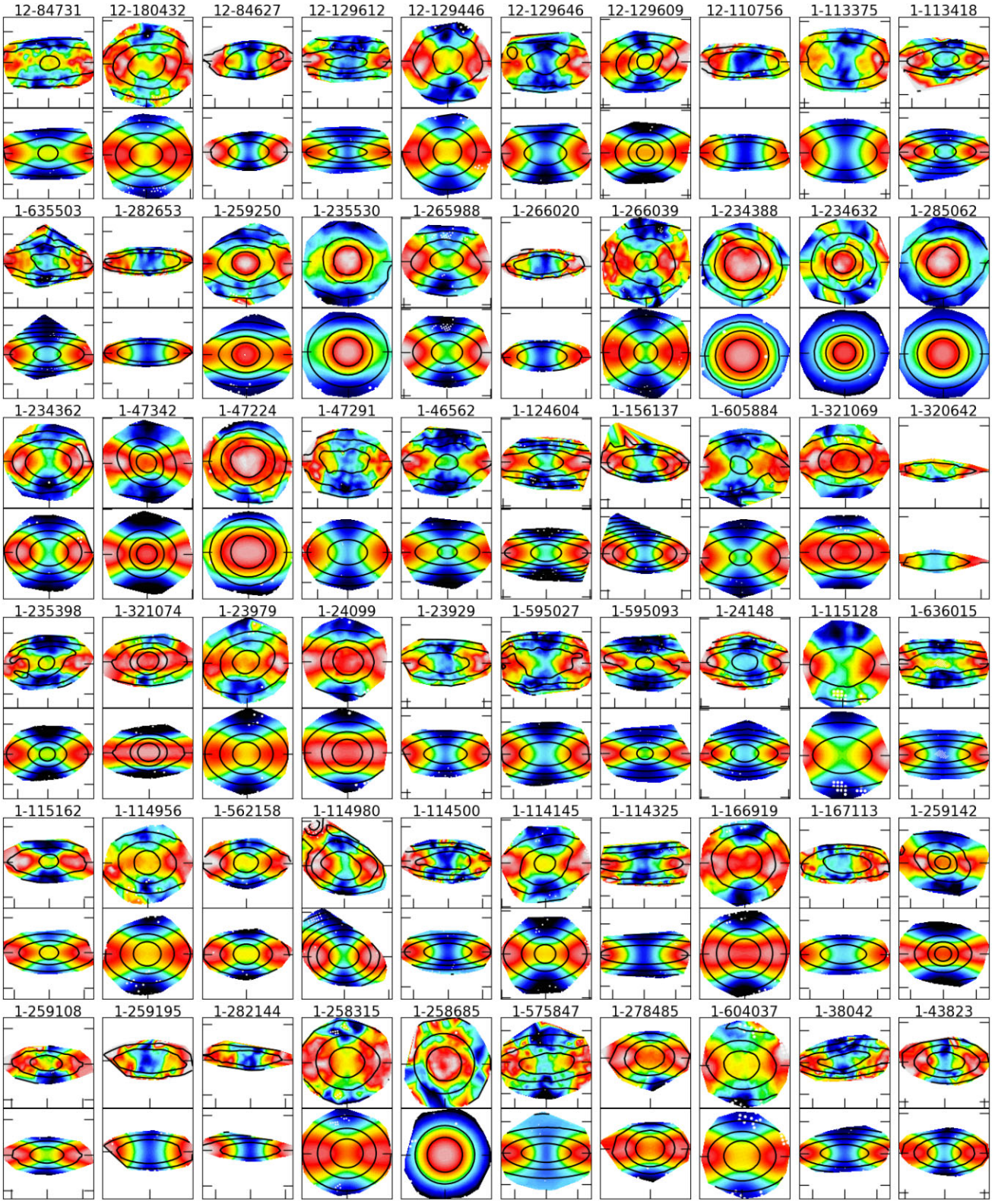

Figure 9. Examples of the mass-follows-light models for Qual = 3 galaxies, using the JAM_{cyl} method. For each galaxy, the top panel shows the observed V_{rms} map, overlaid with the black contours of observed surface brightness (in steps of 1 mag). In the bottom panel, the modelled V_{rms} map and the adopted MGE surface brightness (black contours) are shown. The white circles are the clipped bins, which are not included in the JAM fitting. Ticks are separated by 10 arcsec. The JAM models (the observed and modelled V_{rms} maps) for the full sample can be found in https://manga-dynpop.github.io.

natural choices for splitting ordered and random motions. Our choice corresponds to equation (56) of Cappellari (2020), which is likely better suited for the fast rotator galaxies dominating our sample. After substituting σ_ϕ^2 with σ_R^2 (σ_r^2) in equation (24), the intrinsic first velocity moment $\overline{v_\phi}$ is derived and can be used to predict modelled light-of-sight velocities $\overline{v_{los}}$ (see section 3.1.5 of Cappellari 2008 for more details).

To assess the validity of recovered line-of-sight velocity maps, we calculate the distribution of κ, defined as (Cappellari 2008, equation 52)

$$\kappa = \frac{\sum_k F_k |x'_k V_k|}{\sum_k F_k |x'_k (\overline{v_{los}})_k|}, \tag{26}$$

where F_k is the flux of kth Voronoi bin; V_k and $(\overline{v_{los}})_k$ are the corresponding observed and modelled line-of-sight velocities, respectively; x'_k is the distance of the kth Voronoi bin to the galaxy centre parallel to the major axis. In Fig. 10, we present the distributions of κ for galaxies with different data qualities (Qual $\geqslant 0$, Qual $\geqslant 1$ and Qual $= 3$ from top to bottom). As can be seen, for all models, the distributions of κ peak at $\kappa \approx 1$ regardless of the modelling quality, confirming that, after fitting the density, the first velocity moment can be well predicted under the assumption of an oblate velocity ellipsoid, as first noted in Cappellari (2008) and quantified for a statistical sample of ETGs in Cappellari (2016, fig. 11). Here we find that this empirical fact is valid for all morphological galaxy types and for both $\mathrm{JAM_{cyl}}$ and $\mathrm{JAM_{sph}}$. The rms scatter of the κ distribution decreases from low-quality samples to high-quality samples. If we exclude the Qual $= 0$ galaxies, the rms scatter becomes 8.8 per cent, compatible with the result of ATLAS^{3D} (see fig. 11 in Cappellari 2016). Specifically, the Qual $= 3$ galaxies, which are visually classified as the models that have good fit to the V_{rms} and v_{los}, have a remarkably small observed rms scatter (~ 5 per cent).

6 REALISTIC MODEL UNCERTAINTIES

A key strength of this project is that we derive mass models under two extreme assumptions on the orientation of velocity ellipsoid, namely $\mathrm{JAM_{cyl}}$ and $\mathrm{JAM_{sph}}$. Moreover, for each galaxy in the sample and for each $\mathrm{JAM_{cyl}}$ and $\mathrm{JAM_{sph}}$ model we make four different assumptions for the dark/luminous mass decomposition, resulting in eight different models to analyse the full sample of MaNGA galaxies. In this section, we use the differences between these different model assumptions to assess the level of systematics in our derived dynamical quantities. These dominate the formal (i.e. statistical) uncertainties, which are generally small, unreliable and not very useful for practical usage.

6.1 $\mathrm{JAM_{cyl}}$ versus $\mathrm{JAM_{sph}}$

We focus on five quantities: the mass-weighted total density slope $\overline{\gamma_T}$, the DM fraction $f_{DM}(< R_e)$, the dynamical mass-to-light ratio $(M/L)_e$, and the total mass $M_T(< R_e)$, all four quantities within a sphere of radius R_e, and the reduced chi-square χ^2/DOF (see Section 4 and Appendix B for explanations of these quantities). To reduce the effect of bad fittings, we only use the galaxies of the highest quality (Qual $= 3$) in this test. We perform a linear fit to the quantities obtained with $\mathrm{JAM_{cyl}}$ and $\mathrm{JAM_{sph}}$, using the robust LTS_LINEFIT[12] procedure (Cappellari et al. 2013a), which combines the Least Trimmed Squares robust technique of Rousseeuw & Driessen (2006)

[12]Version 5.0.19, from https://pypi.org/project/ltsfit/.

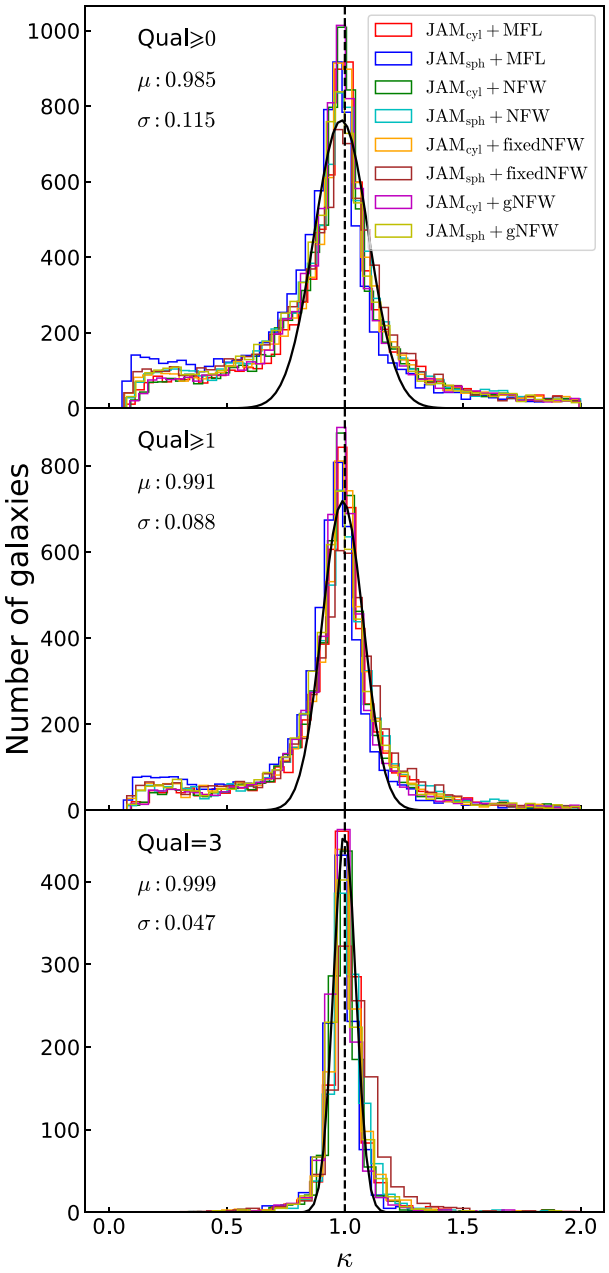

Figure 10. Distributions of the ratio between the observed and the predicted stellar velocities (κ; see Section 5.2 for definition) for galaxies in different modelling quality groups (from top to bottom: Qual $\geqslant 0$, Qual $\geqslant 1$, and Qual $= 3$). In each panel, results for different JAM models are shown with histograms of different colours. The black solid curve is the Gaussian fit of the results for the $\mathrm{JAM_{cyl}}$ + MFL model (for the comparison with Cappellari 2016), with μ and σ being the mean and standard deviation values of the Gaussian distribution.

into a least-squares fitting algorithm which allows for errors in all variables and intrinsic scatter.

The results are presented in Fig. 11. In the bottom panels, the reduced chi-square χ^2/DOF of $\mathrm{JAM_{cyl}}$ and $\mathrm{JAM_{sph}}$ are statistically indistinguishable (with observed rms scatter $\Delta = 0.025$ dex) for NFW and gNFW models, slightly larger than the observed rms scatter ($\Delta = 0.022$ dex) using ATLAS^{3D} data (Cappellari 2020). The observed rms scatter slightly increases to $\Delta = 0.045$ dex for the MFL model and $\Delta = 0.056$ dex for the fixed NFW model, consistent

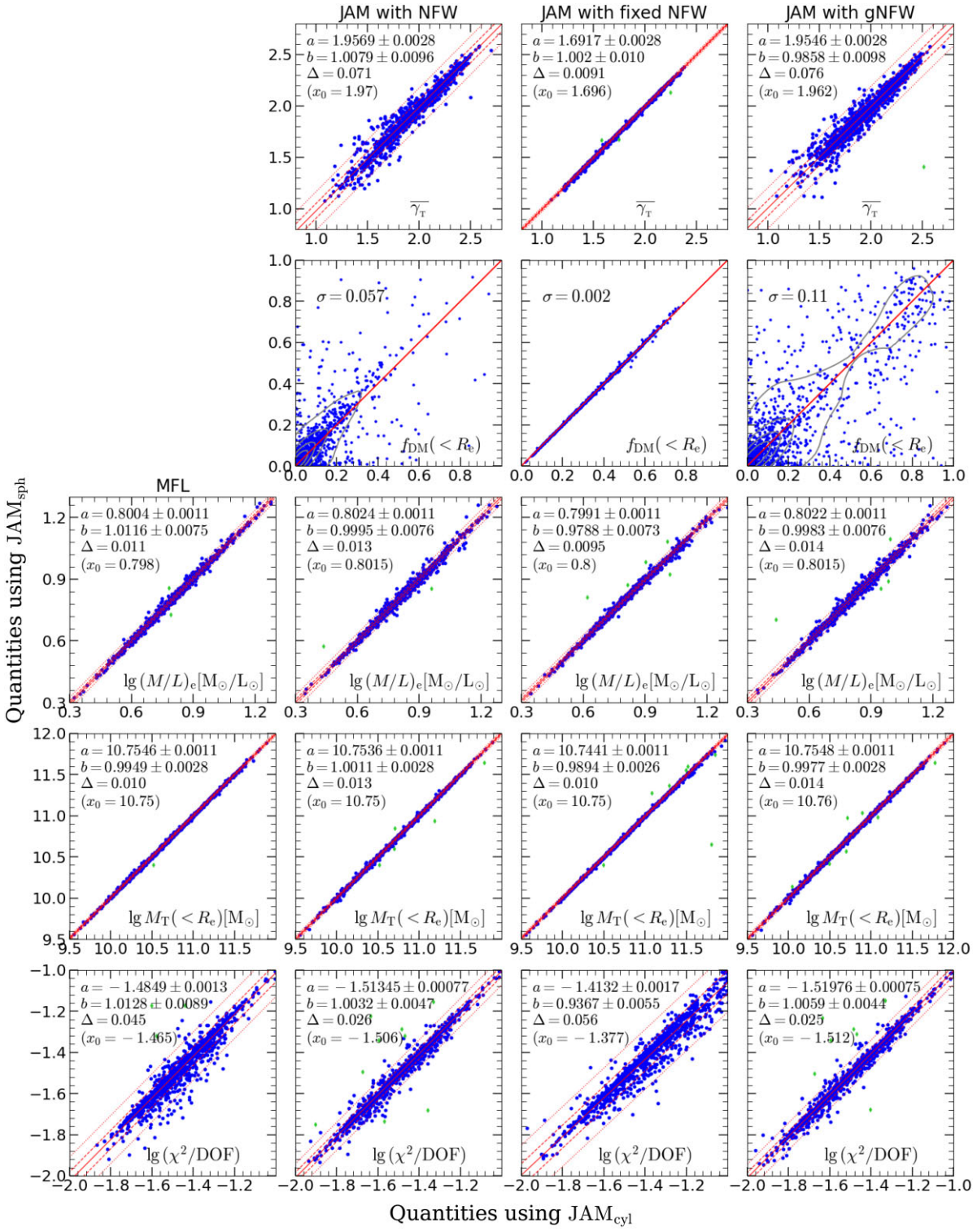

Figure 11. Comparisons of the results derived from JAM$_{\rm cyl}$ (*X*-axis) and from JAM$_{\rm sph}$ (*Y*-axis). The fitting is carried out with least-squares fitting on 1142 galaxies with Qual = 3. Fitting results for MFL, NFW, fixed NFW, and gNFW models (see Section 3.3) are shown from left to right. Four quantities, including the total mass slope $\overline{\gamma_{\rm T}}$, DM fraction within $R_{\rm e}$, $f_{\rm DM}(<R_{\rm e})$, total mass within $R_{\rm e}$, lg $M_{\rm T}(<R_{\rm e})$, and χ^2/DOF are shown from top to bottom. Since the MFL model does not have stellar-DM decomposition, resulting in the equivalent total mass density slope and luminosity density slope, we do not show $\overline{\gamma_{\rm T}}$ and $f_{\rm DM}(<R_{\rm e})$ for the MFL model. In each panel except for the panels of $f_{\rm DM}(<R_{\rm e})$, a linear fit is performed to the parameters derived with different velocity ellipsoid assumptions (i.e. JAM$_{\rm cyl}$ and JAM$_{\rm sph}$), using the LTS_LINEFIT software (Cappellari et al. 2013a) with `clip = 6`. The fitting results are listed in the upper left of each panel. The solid, dashed, and dotted red lines represent the best-fitting, 1σ (68 per cent confidence level) scatter and 2.6σ (99 per cent confidence level) scatter, respectively. The green symbols are the detected outliers beyond 6σ confidence level. In each panel of the second rows, the grey contour is a kernel density estimate of the galaxy distribution (using scipy.stats.gaussian_kde), while the red line is the one-to-one relation. We do not fit the data of $f_{\rm DM}(<R_{\rm e})$ panels. In those cases, the σ represents the 68th percentile of the absolute difference $|f_{\rm DM,\,cyl} - f_{\rm DM,\,sph}|$.

with the expectation that the difference in χ^2/DOF between JAM_{cyl} and JAM_{sph} is smaller for the more flexible mass models.

As shown in the third and fourth rows of Fig. 11, the enclosed dynamical mass-to-light ratio $(M/L)_e$ and the total mass within effective radius $M_T(< R_e)$ are reliable quantities that are nearly unaffected by the assumption of the orientation of velocity ellipsoids. For the MFL model, the rms scatter of $(M/L)_e$ is $\Delta = 0.011$ dex, indicating an error of $\Delta/\sqrt{2} = 1.8$ per cent in the individual $(M/L)_e$. The errors of NFW and gNFW models are ~ 2.1 per cent ($\Delta \approx 0.013$ dex), and the smallest errors are found in the models with fixed NFW dark halo (~ 1.6 per cent, $\Delta \approx 0.0095$ dex).

The mass-weighted total density slopes $\overline{\gamma_T}$ are also very consistent in JAM_{cyl} and JAM_{sph}. The observed rms scatters of NFW, fixed NFW, and gNFW models are $\Delta = 0.071$, $\Delta = 0.0091$, and $\Delta = 0.076$, respectively. The values of observed scatter for NFW and gNFW models are close to those obtained from ATLAS^{3D} ($\Delta = 0.094$, Cappellari 2020, fig. 12), reconfirming the validity of the approach.

When the dark halo slope approaches the slope of the stellar density, a change in the stellar M/L becomes indistinguishable from an increase in the DM fraction. For this reason, one cannot expect to be able to uniquely constrain the $f_{DM}(< R_e)$ in every individual galaxy. Nonetheless, JAM_{cyl} and JAM_{sph} inferred $f_{DM}(< R_e)$ values are statistically consistent, with 1σ scatter of 0.057, 0.0020, and 0.11 for NFW, fixed NFW, and gNFW models, where the 1σ scatter is defined as 68th percentile of the absolute difference $|f_{DM,\,cyl} - f_{DM,\,sph}|$. However, for some extreme cases, the difference can be up to 0.7 between the two different JAM assumptions, which implies the $f_{DM}(< R_e)$ is essentially unconstrained by the data without more restrictive priors. One can also find that different mass models predict different $f_{DM}(< R_e)$, which will be discussed in more detail in Section 6.3. Therefore, when future users analyse DM fractions with our catalogue, it is important to select galaxies with consistent $f_{DM}(< R_e)$ values for different models.

6.2 Uncertainties of density slope, enclosed *M/L*, and mass

We present the scatter of parameters among different models in Fig. 12. The scatter is calculated with respect to the biweight mean (Hoaglin et al. 1983, p. 417) of different models. We compare the values of each model with the biweight mean value, which are shown in Figs 12 and 13. The biweight mean is known as a robust method to determine the central location of a distribution, which is shown to be more robust compared to the conventional mean value (Beers, Flynn & Gebhardt 1990; Andrews & Hampel 2015) in statistics with outliers or small statistical size. With the comparisons between models, we aim to investigate the systematic bias between different models and measure the systematic uncertainties of derived quantities.

On the left column of Fig. 12, the comparisons of mass-weighted total density slopes $\overline{\gamma_T}$ between 6 models are shown (the mass-follows-light models are excluded because that their total density slopes are uniquely decided by their luminosity density slopes, which do not vary with JAM models). For the NFW and gNFW models, the slopes of best-fitting lines are close to unity for Qual $\geqslant 1$ galaxies, while deviations from unity are observed for Qual $= 0$ galaxies. The values of the fixed NFW model deviate from biweight mean values regardless of quality, indicating that the underlying theoretical assumption for the halo is unable to accurately predict the real galaxies. Moreover, the uncertainties of $\overline{\gamma_T}$ between NFW and gNFW models are presented on the left column of Fig. 13 (the fixed NFW model is excluded because they are a theoretical prediction, which we found is not sufficiently reproducing real galaxies). From Qual $= 0$ to Qual $= 3$, the observed rms scatter Δ ranges from 0.19 to 0.049. For the galaxies with Qual > 0, the observed scatters ($\Delta = 0.079$ for Qual $= 1$, $\Delta = 0.034$ for Qual $= 2$, $\Delta = 0.049$ for Qual $= 3$) are compatible with the values $\Delta = 0.13$ obtained by Poci et al. (2017) and $\Delta = 0.094$ obtained by Cappellari (2020). For our alternative definition of total density slope or equation (20), i.e. the logarithmic total density slope γ_T, the rms scatters are nearly identical ($\Delta = 0.18$ for Qual $= 0$, $\Delta = 0.082$ for Qual $= 1$, $\Delta = 0.047$ for Qual $= 2$, $\Delta = 0.049$ for Qual $= 3$; Table 3).

The comparisons of dynamical mass-to-light ratio $(M/L)_e$, total mass within effective radius $M_T(<R_e)$, and total mass within a sphere of 3D half-light radius $M_T(< r_{1/2})$ are presented in the second, third, and fourth columns of Figs 12 and 13. In Fig. 12, for the Qual $= 0$ galaxies, $(M/L)_e$ measurements of the MFL model are systematically smaller compared to other models especially at the high $(M/L)_e$ end. With increasing quality, the systematic difference between different mass models becomes indistinguishable (the correlations between models have a slope of nearly unity except for the Qual $= 2$ galaxies with a significantly small number).

The excellent agreement between MFL and more flexible halo models, with good-quality data, is consistent with the same JAM results for ETGs in ATLAS^{3D} (Cappellari et al. 2013a, fig. 9). While the smaller M/L for MFL models on low-quality data is consistent with the LEGA-C JAM modelling (van Houdt et al. 2021, fig. 9). This is important: Given that with good data the MFL models return the correct $(M/L)_e$, the difference observed at low S/N is unlikely to be a genuine effect. Instead, it must be due to the more flexible halo models being unable to correctly constrain the dark halo and returning overestimated $f_{DM}(< R_e)$ and consequently too large $(M/L)_e$. The tendency of low-quality data to cause overestimated $f_{DM}(< R_e)$ was noted in Cappellari et al. (2013a, fig. 10) and we observe also in this work. We verify that this is not due to galaxies with better data having smaller data coverage and smaller DM fraction. This suggests that, in general, the MFL models provide a more robust estimate of the $(M/L)_e$ than more general models, even in the presence of M/L gradients, and should be preferred with inferior data quality.

Following popular practice, we also compare enclosed masses from different models. However, we stress that these comparisons do not contain any information that is not already better visible in the $(M/L)_e$ plots. In fact, by definition $M_T(<R_e) = L(<R_e) \times (M/L)_e$. This implies that the mass plots can be obtained by multiplying both $x-y$ axes by the same luminosity, effectively stretching the axes' scale and making any differences more difficult to detect. This explains the fact that masses have the same scatter as the M/L within the numerical uncertainties of the clipping process. This is perhaps the reason why masses are often a preferred way of comparing dynamical results than M/L. No apparent systematic differences are observed for the $M_T(< R_e)$, regardless of quality (third column in Fig. 12). The scatters of $(M/L)_e$ and $M_T(< R_e)$ are nearly identical: $\Delta = 0.082$ dex for Qual $= 0$, $\Delta = 0.036$ dex for Qual $= 1$, $\Delta = 0.052$ dex for Qual $= 2$, and $\Delta = 0.018$ dex for Qual $= 3$ (Fig. 13). The larger scatters for Qual $= 2$ galaxies than those for Qual $= 1$ galaxies may be due to the significantly smaller number of Qual $= 2$ galaxies. Moreover, the scatter of $M_T(< R_e)$ for Qual $= 3$ galaxies ($\Delta = 0.018$ dex) is compatible with $\Delta = 0.037$ dex obtained from the full sample of ATLAS^{3D} (Cappellari et al. 2013a), suggesting that models of Qual $= 3$ galaxies are at the same level of accuracy as those of ATLAS^{3D}. The total mass within 3D half-light radius $M_T(< r_{1/2})$ is a robust quantity that has no systematic bias between models (Fig. 12), with a small observed scatter ranging from $\Delta = 0.071$ dex to $\Delta = 0.014$ dex in different quality groups (Fig. 13).

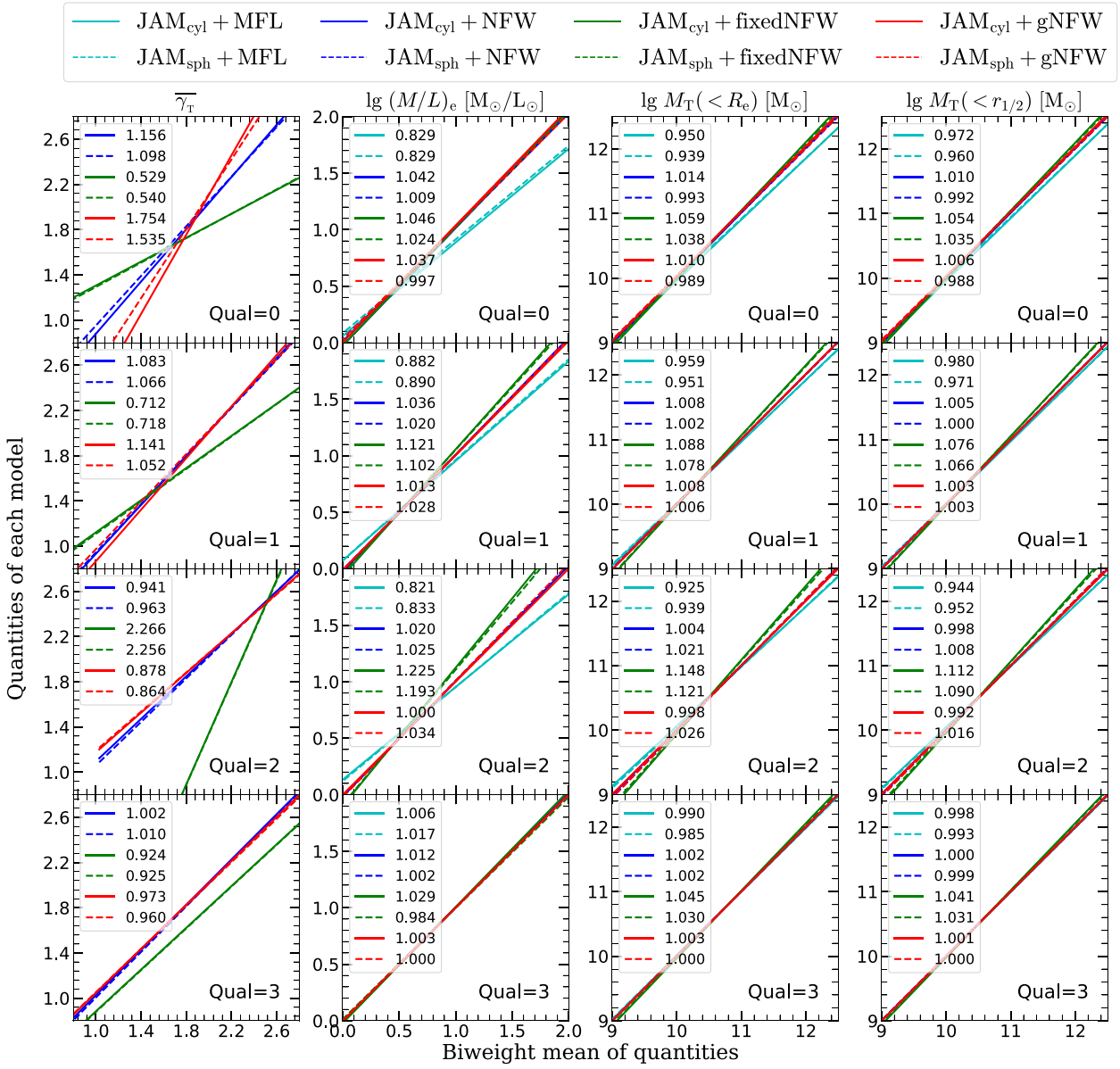

Figure 12. The comparisons of quantities between each model and the biweight mean value of eight models (except for the total density slope $\overline{\gamma_T}$ which does not account for the MFL model) for different quality groups, with best-fitting straight-lines of each model which are derived from LTS_LINEFIT software. Results of galaxies with quality 0, 1, 2, and 3 are shown from top to bottom, and four quantities, including the total density slope $\overline{\gamma_T}$, the dynamical mass-to-light ratio $(M/L)_e$, the total mass within 2D effective radius $M_T(< R_e)$, and the total mass within 3D half-light radius $M_T(<r_{1/2})$ are shown from left to right. The colours correspond to different mass models, while solid and dashed lines represent the JAM$_{cyl}$ and JAM$_{sph}$ methods (see the top legends for the details). Corresponding slopes of best-fitting straight lines for each model are shown in the legend of each panel.

The observed scatters Δ and corresponding errors are presented in Table 3. In summary, the quantities related to the total mass distribution are reliable and no systematic bias between models is observed for the Qual $\geqslant 1$ galaxies (except for the $\overline{\gamma_T}$ inferred from the fixed NFW model). For the Qual $= 0$ galaxies, the total mass within a sphere of R_e or $r_{1/2}$ can still be trusted. The observed rms scatters of quantities significantly decrease with increasing modelling quality, again confirming the importance of our visual quality control and the usefulness of using multiple models to estimate realistic parameter uncertainties. Furthermore, the small scatter also suggests the insensitivity of these quantities to different mass models (i.e. MFL, NFW, fixed NFW, and gNFW models) and different assumptions on the orientation of the velocity ellipsoid (i.e. JAM$_{cyl}$ and JAM$_{sph}$).

6.3 Model uncertainties on DM fractions

Dynamical modelling in general, can only measure total densities, or equivalently enclosed masses. As far as we currently understand, gravity does not distinguish between luminous, baryonic, or DM. For this reason, it is obvious that if one were to allow part of the DM to be distributed like the baryons, any DM decomposition would become degenerate. This implies that the decomposition of the total density into baryonic and DM always necessarily involves some level of assumptions. In practice, we know from numerical simulations, e.g. EAGLE (Crain et al. 2015) and IllustrisTNG (Marinacci et al. 2018; Naiman et al. 2018; Nelson et al. 2018; Pillepich et al. 2018; Springel et al. 2018), that DM is expected to be more extended and smooth than the stars and this allows us to place some constraints

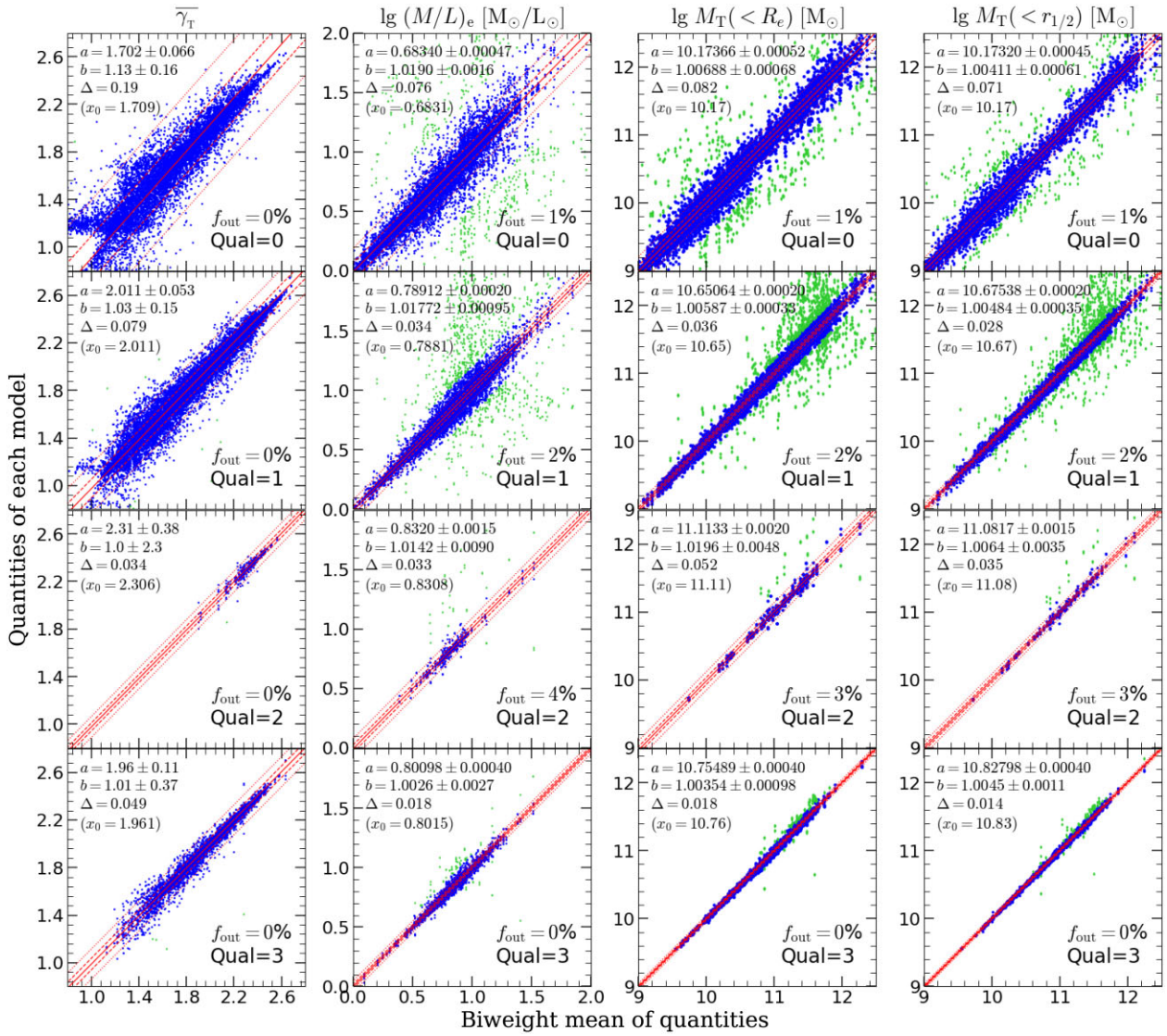

Figure 13. Systematic measurement uncertainties for galaxies in different quality groups. The panels are the same as Fig. 12. In each panel, the *Y*-axis represents the corresponding quality of all 8 models ($\overline{\gamma_T}$ is not shown for MFL and fixed NFW models, since it is uniquely decided by luminosity density slope in the MFL model and values of the fixed NFW model deviate far from other models as shown in Fig. 12), and the X-axis is for the biweight mean value of the quantities (see Section 6.2 for definition) for different models. Using LTS_LINEFIT procedure with `clip = 6`, the best-fitting, 1σ (68 per cent of values) scatter and 2.6σ (99 per cent of values) scatter are fitted and shown with red solid, dashed and dotted lines. The green symbols are the detected outliers beyond 6σ confidence level, while the fraction of the detected outliers are listed in each panel.

Table 3. The errors of individual quantities ($\overline{\gamma_T}$, γ_T, $(M/L)_e$, $M_T(<R_e)$, $M_T(<r_{1/2})$) for different quality groups. The slope and Δ denote the slope and observed scatter obtained by the LTS_LINEFIT procedure. The error is defined as $\Delta/\sqrt{2}$ assuming that the quantities on both axes are comparable. The errors of quantities in this table are derived from eight models listed in Table 1, except for the errors of $\overline{\gamma_T}$ and γ_T, for which MFL and fixed NFW models are not accounted for (see the text in Section 6.2 for more explanations).

Quantities	Qual = 0			Qual = 1			Qual = 2			Qual = 3			Mass models
	Slope	Δ	Error	Slope	Δ	Error	Slope	Δ	Error	Slope	Δ	Error	
$\overline{\gamma_T}$	1.13	0.19	0.13	1.03	0.079	0.056	1.00	0.034	0.024	1.01	0.049	0.035	NFW, gNFW
γ_T	1.10	0.18	0.13	1.02	0.082	0.058	1.00	0.047	0.033	1.01	0.049	0.035	NFW, gNFW
$(M/L)_e$	1.02	0.076 dex	13.2 %	1.02	0.034 dex	5.69 %	1.01	0.033 dex	5.52 %	1.00	0.018 dex	2.97 %	All
$M_T(<R_e)$	1.01	0.082 dex	14.3 %	1.01	0.036 dex	6.04 %	1.02	0.052 dex	8.84 %	1.00	0.018 dex	2.97 %	All
$M_T(<r_{1/2})$	1.00	0.071 dex	12.3 %	1.00	0.028 dex	4.66 %	1.01	0.035 dex	5.86 %	1.00	0.014 dex	2.31 %	All

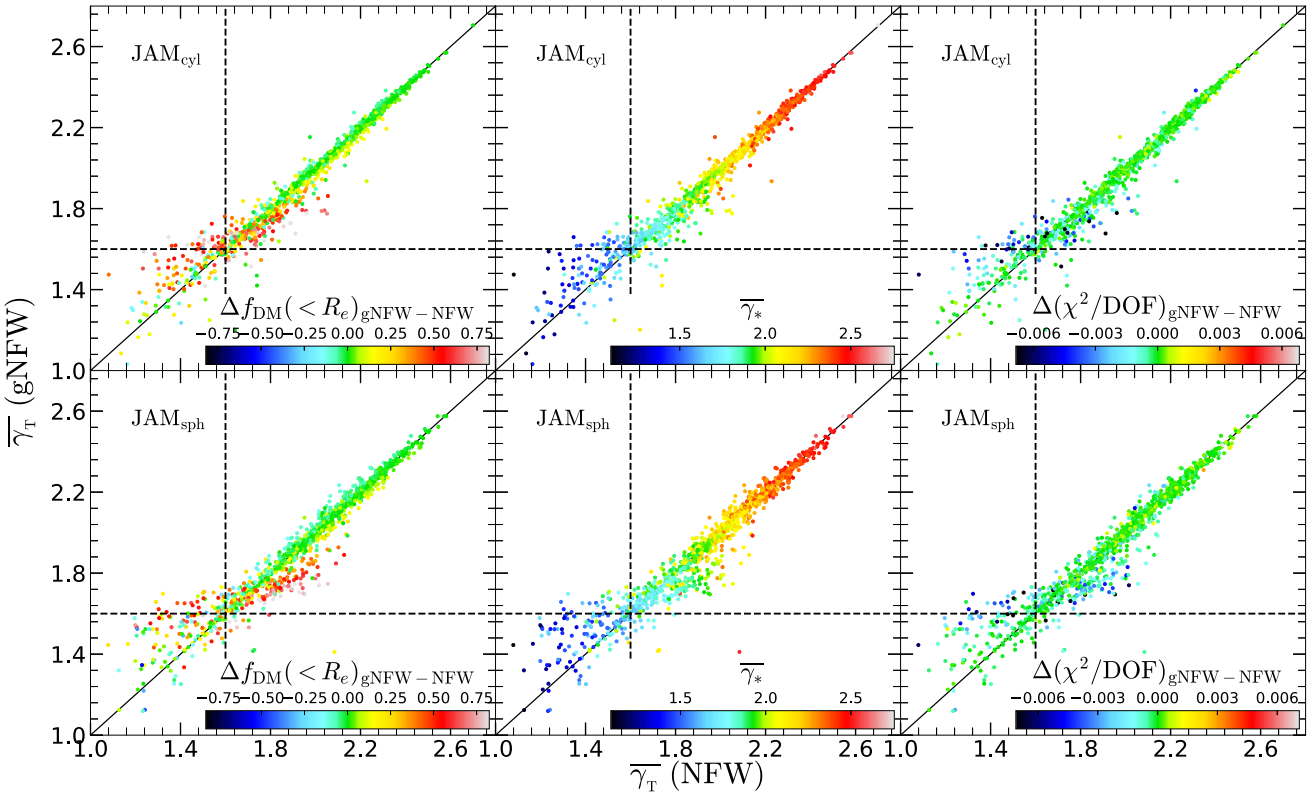

Figure 14. The comparisons of mass-weighted total density slope $\overline{\gamma_{\rm T}}$ derived from NFW models (*X*-axis) and gNFW models (*Y*-axis) for galaxies with Qual = 3, colour-coded by DM difference of the two models ($\Delta f_{\rm DM}(< R_e)_{\rm gNFW\text{-}NFW}$, left panels), stellar density slope ($\overline{\gamma_*}$, middle panels), and χ^2 difference between two models ($\Delta(\chi^2/{\rm DOF})_{\rm gNFW-NFW}$, right panels). Results for JAM$_{\rm cyl}$ and JAM$_{\rm sph}$ are shown in the top and bottom panels, respectively. In each panel, the vertical and horizontal black dashed lines represent the mass-weighted density slope of 1.6, which is approximately the steepest DM density slope (i.e. with the largest absolute value) allowed by the gNFW density profiles (see Table 1, but note that the mass-weighted slope always has a positive sign by definition, as opposed to the inner slope parameter γ of gNFW profiles).

on its contribution. However, these assumptions do not remove all degeneracies and make DM a much more uncertain and assumption-dependent parameter than the other dynamical quantities we can more directly measure.

Using the galaxies of best quality (Qual = 3), the consistency of $f_{\rm DM}(< R_{\rm e})$ between JAM$_{\rm cyl}$ and JAM$_{\rm sph}$ is already shown in the second rows of Fig. 11. Although there is no systematic differences between the inferred values of JAM$_{\rm cyl}$ and JAM$_{\rm sph}$, the non-negligible fraction of outliers makes it necessary to exclude the cases with significant inconsistency when the readers want to use the DM-stellar decomposition results of our modelling.

However, we also notice that there are still some cases in Fig. 11 that have significant differences between different mass models even after excluding the outliers. To understand the origin of the systematic offset of $f_{\rm DM}(< R_{\rm e})$, we present Fig. 14, in which Qual = 3 galaxies are plotted on the $\overline{\gamma_{\rm T}}$(NFW) − $\overline{\gamma_{\rm T}}$(gNFW) plane, colour-coded by the DM fraction difference between NFW and gNFW models, the stellar density slope, and the χ^2/DOF difference between NFW and gNFW models from left to right. Results for JAM$_{\rm cyl}$ and JAM$_{\rm sph}$ are shown in the top and bottom panels, respectively. As can be seen, most galaxies have nearly identical total density slopes and indistinguishable differences in DM fraction under different mass models (i.e. the NFW model versus the gNFW model), while a subset of galaxies has slightly different $\overline{\gamma_{\rm T}}$ and significantly inconsistent $f_{\rm DM}(<R_{\rm e})$. As seen from the right-hand panels of Fig. 14, the χ^2/DOF values of the gNFW model are smaller than those of the NFW model for this subset of galaxies, which is expected due to more free parameters in the gNFW model. For this reason, we use $\overline{\gamma_{\rm T}}$ of the gNFW model as the reference to investigate the origin of the differences in $\overline{\gamma_{\rm T}}$ and $f_{\rm DM}(< R_{\rm e})$ between the two models.

For the galaxies with shallow total and stellar density slopes ($1 < \overline{\gamma_{\rm T}} < 1.6$ and $1 < \overline{\gamma_*} < 1.6$), the variable inner density slope of gNFW profile allows $\overline{\gamma_{\rm DM}}$ to be similar to $\overline{\gamma_*}$ or even steeper. Thus, the DM fraction of the gNFW model can be large for the outliers with $1 < \overline{\gamma_*} < \overline{\gamma_{\rm T}} < 1.6$. But for the NFW model, due to the shallower $\overline{\gamma_{\rm DM}}$, the only way to reach the same total density slope as the gNFW model is to reduce the DM fraction. However, it is still impossible to reach a steeper $\overline{\gamma_{\rm T}}$ than $\overline{\gamma_*}$ for the NFW model even with very small DM fraction, leading to the much smaller $f_{\rm DM}(< R_{\rm e})$ and slightly shallower $\overline{\gamma_{\rm T}}$ of the NFW model (see the left-hand panels of Fig. 14).

Meanwhile, the stellar density slope $\overline{\gamma_*}$ is always steeper than $\overline{\gamma_{\rm DM}}$ for the galaxies with $1.6 < \overline{\gamma_{\rm T}} < 2$. Since the total density slope $\overline{\gamma_{\rm T}}$ is determined by the interplay between shallower DM density slope $\overline{\gamma_{\rm DM}}$ and steeper stellar density slope $\overline{\gamma_*}$, the DM fraction in the gNFW model can be higher responding to the steeper $\overline{\gamma_{\rm DM}}$. For the galaxies with steeper total density slopes ($\overline{\gamma_{\rm T}} > 2$), no distinguishable differences in $\overline{\gamma_{\rm T}}$ and $f_{\rm DM}(< R_{\rm e})$ between NFW and gNFW models are observed.

7 SUMMARY

In this work, we construct a full catalogue of dynamical quantities for the complete sample of 10K galaxies with integral-field kinematics from the MaNGA survey (SDSS DR17; Abdurro'uf et al. 2022) with

their fitting quality carefully assessed. The quantities are derived using a detailed dynamical model (JAM; Cappellari 2008, 2020), which is based on the axisymmetric Jeans equations and had been demonstrated by others to be more accurate than other more-general techniques in recovering the total mass distribution. Four mass models (i.e. MFL, NFW, fixed NFW, and gNFW; see Section 3.3 for details) and two assumptions on the orientation of velocity ellipsoid (i.e. the cylindrically-aligned $\mathrm{JAM_{cyl}}$ and the spherically-aligned $\mathrm{JAM_{sph}}$ velocity ellipsoids; see Section 3.1) are adopted in this work. By fitting the observed second velocity moments $V_{\rm rms}$, the free parameters of different models are optimized to find the maximum likelihood value. Based on the comparison between observed and modelled $V_{\rm rms}$ and V maps, the sample is visually classified into different modelling quality groups (Qual $= -1$, 0, 1, 2, 3; see Section 5.1).

The main results of tests on the robustness of measured quantities [e.g. mass-weighted total density slope $\overline{\gamma_{\rm T}}$, dynamical mass-to-light ratio $(M/L)_{\rm e}$, enclosed total mass within a sphere of $R_{\rm e}$ $M_{\rm T}(< R_{\rm e})$, enclosed total mass within a sphere of $r_{1/2}$ $M_{\rm T}(< r_{1/2})$; see Section 4 for details] and the systematic uncertainties in different models are as follows:

(i) As shown in Fig. 10, the first-order velocity moments can be well recovered ($\kappa \approx 1$) under the assumption of oblate velocity ellipsoid, regardless of modelling quality. The rms scatter of κ distribution decreases with the improvement of modelling quality and has a remarkably small scatter of 0.05 for the Qual $= 3$ galaxies.

(ii) The comparisons between quantities inferred from $\mathrm{JAM_{cyl}}$ and $\mathrm{JAM_{sph}}$ in Fig. 11 show that no systematic offsets between these two methods. The small observed scatter of $\overline{\gamma_{\rm T}}$ ($\Delta \approx 0.071 - 0.076$), $f_{\rm DM}(< R_{\rm e})$ (1σ scatter of 0.057 for the NFW model, 1σ scatter of 0.11 for the gNFW model), $M_{\rm T}(< R_{\rm e})$ ($\Delta \approx 0.010-0.014$ dex), and χ^2/DOF ($\Delta \approx 0.025-0.045$ dex) are comparable to the values obtained in Cappellari (2020), reconfirming the validity of these two approaches.

(iii) Systematic bias and errors are explored by comparing measured quantities of eight different models (four mass models with different assumptions on the DM haloes and two assumptions on the orientation of velocity ellipsoid for each mass model). No distinguishable systematic differences in $\overline{\gamma_{\rm T}}$ (MFL and fixed NFW models are excluded), $(M/L)_{\rm e}$, $M_{\rm T}(< R_{\rm e})$, and $M_{\rm T}(< r_{1/2})$ are observed for different modelling qualities (the slopes of best-fitting straight lines in Fig. 12 are close to 1). The enclosed masses computed with MFL models are highly consistent with those computed with more flexible models with DM, when the data are good. However, models with DM can provide significantly larger enclosed masses on low-quality data. The fixed NFW model inferred $\overline{\gamma_{\rm T}}$ values systematically deviate from other models due to its fixed-halo assumption, thus are not recommended for use. The systematic errors for the galaxies of different modelling qualities are listed in Table 3. The small observed rms scatters shown in Fig. 13 suggest that the quantities related to total mass distribution are reliable for Qual $\geqslant 1$ galaxies. Specifically, the enclosed total mass within a sphere of $R_{\rm e}$ or $r_{1/2}$ for Qual $= 0$ galaxies can be used by selecting the consistent values between models.

(iv) The DM fraction $f_{\rm DM}(<R_{\rm e})$ are consistent between different models for most galaxies. However, a systematic offset of $f_{\rm DM}(< R_{\rm e})$ between different mass models is reported for a subset of galaxies (left columns in Fig. 14). The inconsistency for this subset of galaxies is due to the fact that the DM profile of gNFW is more flexible in contributing to the total density profile as discussed in Section 6.3.

Thanks to the large sample of MaNGA survey, this catalogue provides robust dynamical modelling for ∼10 000 galaxies, which makes it the largest catalogue of galaxies with dynamical properties so far. The MaNGA survey consists of different types of nearby galaxies, providing an unbiased and representative sample to study the relations related to stellar dynamics (e.g. FP, mass–size plane, total density slopes, DM fractions, IMF variations). Furthermore, we expect that this catalogue solely or combined with stellar population analysis, e.g. FIREFLY (Goddard et al. 2017; Neumann et al. 2022), Pipe3D (Sánchez et al. 2022), and pPXF (Lu et al. 2023, Paper II), will bring new insights into our understanding of galaxy formation and evolution. In the following papers of this project, we will present a catalogue of stellar population properties (Lu et al. 2023, Paper II), the dynamical scaling relations (Zhu et al. 2023, Paper III), the combined analysis with weak gravitational lensing (Wang et al. 2023, Paper IV), and the IMF variations (Lu et al. in preparation).

SOFTWARE CITATIONS

This work uses the following software packages:

(i) ASTROPY (Astropy Collaboration 2013, 2018)
(ii) PYMULTINEST (Buchner et al. 2014)
(iii) MATPLOTLIB (Hunter 2007)
(iv) NUMPY (van der Walt, Colbert & Varoquaux 2011; Harris et al. 2020)
(v) PYTHON (Van Rossum & Drake 2009)
(vi) SCIKIT-IMAGE (van der Walt et al. 2014)
(vii) SCIPY (Virtanen et al. 2020)
(viii) JAMPY (Cappellari 2008, 2020)
(ix) MGEFIT (Cappellari 2002)
(x) PAFIT (Krajnović et al. 2006)
(xi) LTSFIT (Cappellari et al. 2013a)

ACKNOWLEDGEMENTS

We acknowledge Dr Dandan Xu for helpful discussions on this paper. This work is partly supported by the National Key Research and Development Program of China (number 2018YFA0404501 to SM), by the National Science Foundation of China (grant numbers 11821303, 11761131004, and 11761141012). This project is also partly supported by Tsinghua University Initiative Scientific Research Program ID 2019Z07L02017. We also acknowledge the science research grants from the China Manned Space Project with number CMS-CSST-2021-A11. KZ and RL acknowledge the support of National Nature Science Foundation of China (grant numbers 11988101, 11773032, and 12022306), the support from the Ministry of Science and Technology of China (grant number 2020SKA0110100), the science research grants from the China Manned Space Project (numbers CMS-CSST-2021-B01 and CMS-CSST-2021-A01), CAS Project for Young Scientists in Basic Research (number YSBR-062), and the support from K.C. Wong Education Foundation.

Funding for the SDSS-IV has been provided by the Alfred P. Sloan Foundation, the U.S. Department of Energy Office of Science, and the Participating Institutions.

SDSS-IV acknowledges support and resources from the Center for High Performance Computing at the University of Utah. The SDSS website is www.sdss.org.

SDSS-IV is managed by the Astrophysical Research Consortium for the Participating Institutions of the SDSS Collaboration including the Brazilian Participation Group, the Carnegie

Institution for Science, Carnegie Mellon University, Center for Astrophysics|Harvard & Smithsonian, the Chilean Participation Group, the French Participation Group, Instituto de Astrofísica de Canarias, The Johns Hopkins University, Kavli Institute for the Physics and Mathematics of the Universe (IPMU)/University of Tokyo, the Korean Participation Group, Lawrence Berkeley National Laboratory, Leibniz Institut für Astrophysik Potsdam (AIP), Max-Planck-Institut für Astronomie (MPIA Heidelberg), Max-Planck-Institut für Astrophysik (MPA Garching), Max-Planck-Institut für Extraterrestrische Physik (MPE), National Astronomical Observatories of China, New Mexico State University, New York University, University of Notre Dame, Observatário Nacional/MCTI, The Ohio State University, Pennsylvania State University, Shanghai Astronomical Observatory, United Kingdom Participation Group, Universidad Nacional Autónoma de México, University of Arizona, University of Colorado Boulder, University of Oxford, University of Portsmouth, University of Utah, University of Virginia, University of Washington, University of Wisconsin, Vanderbilt University, and Yale University.

DATA AVAILABILITY

The analysis results (including the catalogue and the figures of model fitting) are publicly available as supplementary files on the journal website. The catalogue is a single FITS file (∼20 MB), while the data model is presented in Appendix B. The full data release including the catalogue, more supplementary files (e.g. the mass profiles), and the updates (if any) on the catalogue will be posted in https://manga-dynpop.github.io. The MaNGA kinematics data are publicly available in https://www.sdss4.org/dr17/manga/manga-data/data-access/ and the corresponding imaging data is available in https://www.sdss.org/dr12/imaging/images/.

REFERENCES

Abadi M. G., Navarro J. F., Fardal M., Babul A., Steinmetz M., 2010, MNRAS, 407, 435
Abdurro'uf et al., 2022, ApJS, 259, 35
Abolfathi B. et al., 2018, ApJS, 235, 42
Alam S. et al., 2015, ApJS, 219, 12
Andrews D. F., Hampel F. R., 2015, Robust Estimates of Location: Survey and Advances. Princeton Univ. Press, Princeton, NJ
Astropy Collaboration, 2013, A&A, 558, A33
Astropy Collaboration, 2018, AJ, 156, 123
Auger M. W., Treu T., Bolton A. S., Gavazzi R., Koopmans L. V. E., Marshall P. J., Moustakas L. A., Burles S., 2010, ApJ, 724, 511
Beers T. C., Flynn K., Gebhardt K., 1990, AJ, 100, 32
Belfiore F. et al., 2019, AJ, 158, 160
Binney J., 2005, MNRAS, 363, 937
Binney J., 2010, MNRAS, 401, 2318
Binney J., Mamon G. A., 1982, MNRAS, 200, 361
Binney J., Tremaine S., 1987, Galactic Dynamics. Princeton Univ. Press, Princeton, NJ
Blanton M. R., Roweis S., 2007, AJ, 133, 734
Blanton M. R., Kazin E., Muna D., Weaver B. A., Price-Whelan A., 2011, AJ, 142, 31
Bosma A., 1981, AJ, 86, 1825
Bosma A., van der Kruit P. C., 1979, A&A, 79, 281
Bovy J., 2014, ApJ, 795, 95
Bryant J. J. et al., 2015, MNRAS, 447, 2857
Buchner J. et al., 2014, A&A, 564, A125
Bundy K. et al., 2015, ApJ, 798, 7
Cappellari M., 2002, MNRAS, 333, 400
Cappellari M., 2008, MNRAS, 390, 71
Cappellari M., 2016, ARA&A, 54, 597
Cappellari M., 2017, MNRAS, 466, 798
Cappellari M., 2020, MNRAS, 494, 4819
Cappellari M., 2022, preprint (arXiv:2208.14974)
Cappellari M., Copin Y., 2003, MNRAS, 342, 345
Cappellari M., Emsellem E., 2004, PASP, 116, 138
Cappellari M. et al., 2006, MNRAS, 366, 1126
Cappellari M. et al., 2007, MNRAS, 379, 418
Cappellari M. et al., 2011, MNRAS, 413, 813
Cappellari M. et al., 2012, Nature, 484, 485
Cappellari M. et al., 2013a, MNRAS, 432, 1709
Cappellari M. et al., 2013b, MNRAS, 432, 1862
Cappellari M. et al., 2015, ApJ, 804, L21
Ciotti L., 1991, A&A, 249, 99
Crain R. A. et al., 2015, MNRAS, 450, 1937
de Lorenzi F., Debattista V. P., Gerhard O., Sambhus N., 2007, MNRAS, 376, 71
de Vaucouleurs G., de Vaucouleurs A., Corwin H. G. J., Buta R. J., Paturel G., Fouque P., 1991, Third Reference Catalogue of Bright Galaxies. Springer, New York
de Zeeuw P. T. et al., 2002, MNRAS, 329, 513
Drory N. et al., 2015, AJ, 149, 77
Duffy A. R., Schaye J., Kay S. T., Dalla Vecchia C., Battye R. A., Booth C. M., 2010, MNRAS, 405, 2161
Dutton A. A., Macciò A. V., 2014, MNRAS, 441, 3359
Dutton A. A., Treu T., 2014, MNRAS, 438, 3594
Emsellem E., Monnet G., Bacon R., 1994, A&A, 285, 723
Emsellem E. et al., 2007, MNRAS, 379, 401
Emsellem E. et al., 2011, MNRAS, 414, 888
Falcón-Barroso J., Sánchez-Blázquez P., Vazdekis A., Ricciardelli E., Cardiel N., Cenarro A. J., Gorgas J., Peletier R. F., 2011, A&A, 532, A95
Feroz F., Hobson M. P., Bridges M., 2009, MNRAS, 398, 1601
Feroz F., Hobson M. P., Cameron E., Pettitt A. N., 2019, Open J. Astrophys., 2, 10
Gablonsky J., Kelley C., 2001, J. Global Opt., 21, 27
Gebhardt K. et al., 2001, AJ, 122, 2469
Gebhardt K. et al., 2003, ApJ, 583, 92
Gerhard O. E., 1993, MNRAS, 265, 213
Gerhard O., Kronawitter A., Saglia R. P., Bender R., 2001, AJ, 121, 1936
Goddard D. et al., 2017, MNRAS, 466, 4731
Graham M. T. et al., 2018, MNRAS, 477, 4711
Gunn J. E. et al., 2006, AJ, 131, 2332
Häfner R., Evans N. W., Dehnen W., Binney J., 2000, MNRAS, 314, 433
Harris C. R. et al., 2020, Nature, 585, 357
Hoaglin D. C., Mosteller F., Tukey J. W., 1983, in Hoaglin D. C., Mosteller F., Tukey J. W., eds, Understanding Robust and Exploratory Data Analysis: Wiley Series in Probability and Mathematical Statistics. Wiley, New York
Hogg D. W., Baldry I. K., Blanton M. R., Eisenstein D. J., 2002, preprint (arXiv:astro-ph/0210394)
Hunt J. A. S., Kawata D., 2014, MNRAS, 443, 2112
Hunter J. D., 2007, Comput. Sci. Eng., 9, 90
Jin Y., Zhu L., Long R. J., Mao S., Xu D., Li H., van de Ven G., 2019, MNRAS, 486, 4753
Jones D. R., Perttunen C. D., Stuckman B. E., 1993, J. Opt. Theor. Appl., 79, 157
Krajnović D., Cappellari M., de Zeeuw P. T., Copin Y., 2006, MNRAS, 366, 787
Krajnović D. et al., 2011, MNRAS, 414, 2923
Krajnović D., Emsellem E., den Brok M., Marino R. A., Schmidt K. B., Steinmetz M., Weilbacher P. M., 2018, MNRAS, 477, 5327
Lablanche P.-Y. et al., 2012, MNRAS, 424, 1495
Laporte C. F. P., White S. D. M., Naab T., Ruszkowski M., Springel V., 2012, MNRAS, 424, 747
Law D. R. et al., 2015, AJ, 150, 19
Law D. R. et al., 2016, AJ, 152, 83
Law D. R. et al., 2021, AJ, 161, 52
Leung G. Y. C. et al., 2018, MNRAS, 477, 254
Li H., Li R., Mao S., Xu D., Long R. J., Emsellem E., 2016, MNRAS, 455, 3680

Li H. et al., 2017, ApJ, 838, 77
Li H. et al., 2018a, MNRAS, 476, 1765
Li H., Mao S., Cappellari M., Graham M. T., Emsellem E., Long R. J., 2018b, ApJ, 863, L19
Li R. et al., 2019, MNRAS, 490, 2124
Long R. J., Mao S., 2010, MNRAS, 405, 301
Long R. J., Mao S., 2018, Res. Astron. Astrophys., 18, 145
Loubser S. I., Babul A., Hoekstra H., Bahé Y. M., O'Sullivan E., Donahue M., 2020, MNRAS, 496, 1857
Loubser S. I., Hoekstra H., Babul A., Bahé Y. M., Donahue M., 2021, MNRAS, 500, 4153
Lu S., Zhu K., Cappellari M., Li R., Mao S., Xu D., 2023, MNRAS, preprint (arXiv:2304.11712)
Marinacci F. et al., 2018, MNRAS, 480, 5113
McConnell N. J., Ma C.-P., Gebhardt K., Wright S. A., Murphy J. D., Lauer T. R., Graham J. R., Richstone D. O., 2011, Nature, 480, 215
Mitzkus M., Cappellari M., Walcher C. J., 2017, MNRAS, 464, 4789
Monnet G., Bacon R., Emsellem E., 1992, A&A, 253, 366
Moster B. P., Naab T., White S. D. M., 2013, MNRAS, 428, 3121
Naiman J. P. et al., 2018, MNRAS, 477, 1206
Navarro J. F., Frenk C. S., White S. D. M., 1996, ApJ, 462, 563
Nelson D. et al., 2018, MNRAS, 475, 624
Neumann J. et al., 2022, MNRAS, 513, 5988
Neureiter B. et al., 2021, MNRAS, 500, 1437
Oort J. H., 1940, ApJ, 91, 273
Pillepich A. et al., 2018, MNRAS, 475, 648
Planck Collaboration XIII, 2016, A&A, 594, A13
Poci A., Cappellari M., McDermid R. M., 2017, MNRAS, 467, 1397
Rousseeuw P., Driessen K., 2006, Data Min. Knowl. Discov., 12, 29
Rubin V. C., Ford W. Kent J., 1970, ApJ, 159, 379
Rubin V. C., Ford W. K. J., Thonnard N., 1980, ApJ, 238, 471
Rubin V. C., Ford W. K. J., Thonnard N., Burstein D., 1982, ApJ, 261, 439
Rubin V. C., Burstein D., Ford W. K. J., Thonnard N., 1985, ApJ, 289, 81
Rubin V. C., Whitmore B. C., Ford W. Kent J., 1988, ApJ, 333, 522
Sánchez-Blázquez P. et al., 2006, MNRAS, 371, 703
Sánchez S. F. et al., 2012, A&A, 538, A8
Sánchez S. F. et al., 2022, ApJSS, 262, 36
Schwarzschild M., 1979, ApJ, 232, 236
Scott N. et al., 2013, MNRAS, 432, 1894
Scott N. et al., 2015, MNRAS, 451, 2723
Shetty S., Cappellari M., McDermid R. M., Krajnović D., de Zeeuw P. T., Davies R. L., Kobayashi C., 2020, MNRAS, 494, 5619
Skrutskie M. F. et al., 2006, AJ, 131, 1163
Smee S. A. et al., 2013, AJ, 146, 32
Springel V. et al., 2018, MNRAS, 475, 676
Stoughton C. et al., 2002, AJ, 123, 485
Syer D., Tremaine S., 1996, MNRAS, 282, 223
Thomas J. et al., 2009, MNRAS, 393, 641
Van Rossum G., Drake F. L., 2009, Python 3 Reference Manual. CreateSpace, Scotts Valley, CA
van den Bosch R. C. E., van de Ven G., 2009, MNRAS, 398, 1117
van den Bosch R. C. E., van de Ven G., Verolme E. K., Cappellari M., de Zeeuw P. T., 2008, MNRAS, 385, 647
van Houdt J. et al., 2021, ApJ, 923, 11
van der Walt S., Colbert S. C., Varoquaux G., 2011, Comput. Sci. Eng., 13, 22
van der Walt S. et al., 2014, PeerJ, 2, e453
Virtanen P. et al., 2020, Nat. Methods, 17, 261
Wake D. A. et al., 2017, AJ, 154, 86
Wang B., Cappellari M., Peng Y., 2021, MNRAS, 500, L27
Wang C. et al., 2023, MNRAS, preprint (arXiv:2304.11715)
Westfall K. B. et al., 2019, AJ, 158, 231
White S. D. M., Frenk C. S., 1991, ApJ, 379, 52
White S. D. M., Rees M. J., 1978, MNRAS, 183, 341
Willmer C. N. A., 2018, ApJS, 236, 47
Wyithe J. S. B., Turner E. L., Spergel D. N., 2001, ApJ, 555, 504
Yan R. et al., 2016, AJ, 151, 8
Zhu L. et al., 2014, ApJ, 792, 59
Zhu L. et al., 2018, Nat. Astron., 2, 233
Zhu L. et al., 2020, MNRAS, 496, 1579
Zhu L. et al., 2022, A&A, 664, A115
Zhu K., Lu S., Cappellari M., Li R., Mao S., Gao L., 2023, MNRAS, preprint (arXiv:2304.11714)
Zwicky F., 1933, Helvetica Phys. Acta, 6, 110
Zwicky F., 1937, ApJ, 86, 217
Zwicky F., 2009, Gen. Rel. Grav., 41, 207

SUPPORTING INFORMATION

Supplementary data are available at *MNRAS* online.

SDSSDR17_MaNGA_JAM.fits.zip

Please note: Oxford University Press is not responsible for the content or functionality of any supporting materials supplied by the authors. Any queries (other than missing material) should be directed to the corresponding author for the article.

APPENDIX A: MEASURING THE AXIAL RATIO OF DUST RING

We perform MGE fitting on the images of the dust ring galaxies and derive the residual maps by subtracting the MGE models from the images. The ring structure cannot be modelled by MGE (the surface brightness of Gaussians always decreases with increasing radius, while the ring structure results in a bump on the surface brightness profile), thus the ring structure is presented in the residual map. Then we extract the ring by (1) roughly selecting an ellipse shell that contains the ring structure by eye, (2) selecting the brightest 5–20 per cent (typically 10 per cent) pixels within the ellipse shell, and (3) masking the foreground stars by hand if necessary. We use the least-squares estimator for 2D ellipses, skimage.measure.EllipseModel (SCIKIT-IMAGE; Walt et al. 2014), to obtain the best-fitting ellipse model and then iteratively increase/decrease the axial ratio of the ellipse, with the centre, the semiminor axis, and the position angle of the best-fitting ellipse fixed, until the residuals increase by 10 per cent (see Fig. A1). In this way, we are able to obtain the upper and the lower limit of the observed axial ratio of the dust ring, with which the range of galaxy inclination can be calculated.

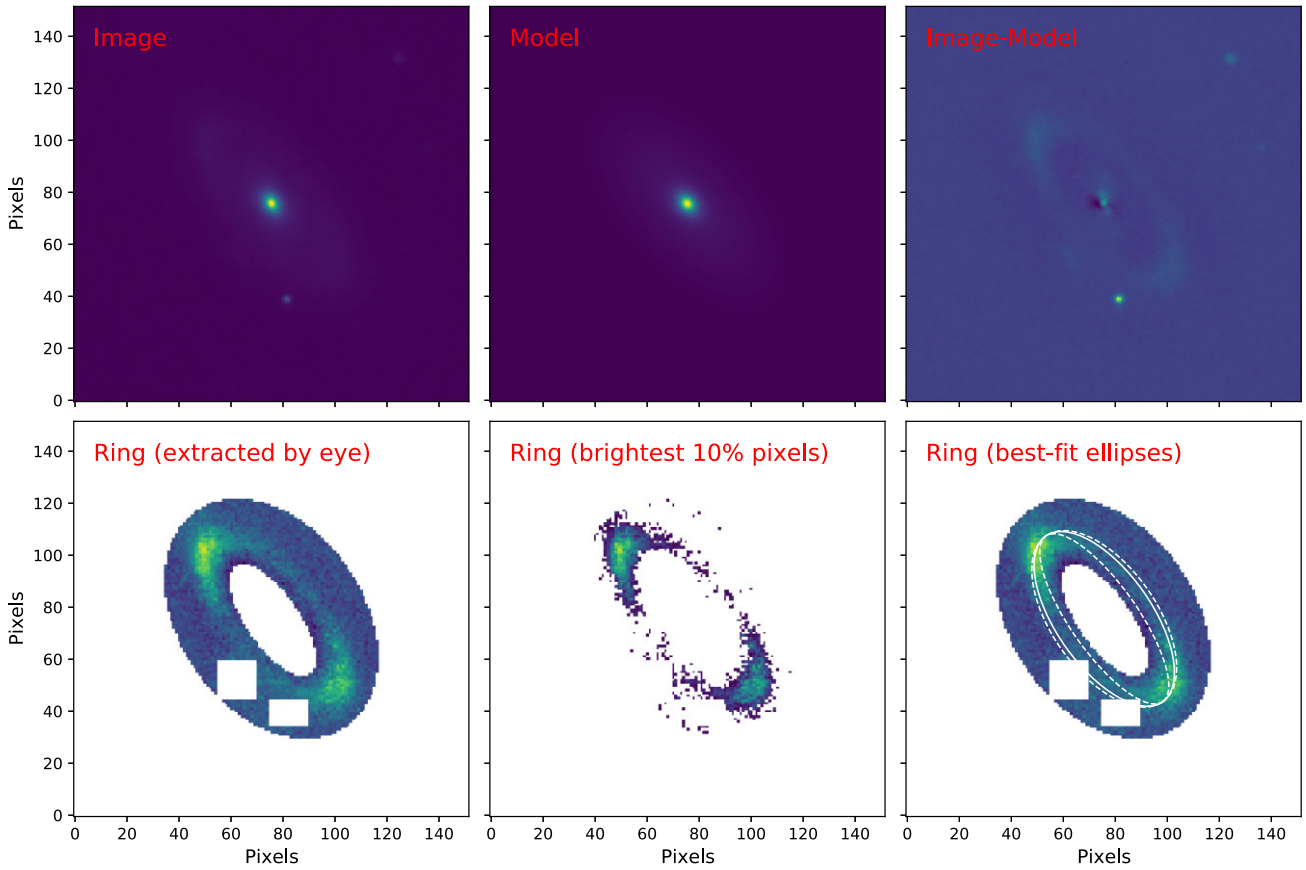

Figure A1. An example of measuring the axial ratio of the dust ring for the galaxy 8341-6101. From left to right and top to bottom, the image, the MGE model, the residual map (image-model), the ring structure extracted by eye, the brightest 10 per cent pixels of the extracted ring structure which are used to obtain the best-fitting ellipse, and the ring structure overlaid with best-fitting ellipses. The white solid line in the bottom right-hand panel is the best-fitting ellipse, while the white dashed lines are the ellipses that have 10 per cent larger residuals than the best-fitting one.

APPENDIX B: PROPERTIES INCLUDED IN THE CATALOGUE

We present the data model of this catalogue in Table B1, which lists the dynamical properties derived from the analysis described in this paper.

Table B1. Dynamical properties for each model. For each property, the Header Data Unit (HDU) in which it is stored, the name, its units, and a brief description are presented. The HDU ranging from 2 to 9 correspond to models $\mathrm{JAM_{cyl}}$ + MFL, $\mathrm{JAM_{sph}}$ + MFL, $\mathrm{JAM_{cyl}}$ + NFW, $\mathrm{JAM_{sph}}$ + NFW, $\mathrm{JAM_{cyl}}$ + fixedNFW, $\mathrm{JAM_{sph}}$ + fixedNFW, $\mathrm{JAM_{cyl}}$ + gNFW, $\mathrm{JAM_{sph}}$ + gNFW. The NFW profile is written as $\rho_{\rm DM}(r) = \rho_s \left(\frac{r}{r_s}\right)^{-1} \left(\frac{1}{2} + \frac{1}{2}\frac{r}{r_s}\right)^{-2}$, while the gNFW profile is written as $\rho_{\rm DM}(r) = \rho_s \left(\frac{r}{r_s}\right)^{\gamma} \left(\frac{1}{2} + \frac{1}{2}\frac{r}{r_s}\right)^{-\gamma-3}$. The properties with prefix 'nsa_' are taken from the NSA catalogue (Blanton & Roweis 2007; Blanton et al. 2011).

HDU (1)	Name (2)	Units (3)	Description (4)
0	Primary		Empty primary header
1	plate		The plate ID (e.g. 7443)
	ifudsgn		The IFU design ID (e.g.12703)
	plateifu		The plate + ifudsgn name (e.g. 7443-12703)
	mangaid		Unique MaNGA ID (e.g. 1-114145)
	obj_ra	degree	Right ascension of the science object in J2000
	obj_dec	degree	Declination of the science object in J2000
	ebvgal		$E(B-V)$ value from sdss dust routine for this IFU
	target		Flag for subsample of MaNGA (primary: 0, secondary: 1, colour enhanced: 2)
	rmax_arcsec	arcsec	The kinematic data range, which is defined as the largest radius of the Voronoi bins
	DA	Mpc	Adopted angular-diameter distance, with a flat Universe of $\Omega_{\rm m} = 0.307$, $h = 0.677$ (Planck Collaboration XIII 2016)
	Re_arcsec_MGE	arcsec	Effective radius (projected circular half-light radius from MGE fitting, in SDSS *r* band)
	Rmaj_arcsec_MGE	arcsec	Major axis of elliptical half-light isophote from MGE fitting, in SDSS *r* band
	Lum_tot_MGE	$\lg(\mathrm{L_\odot})$	Total luminosity from MGE fitting, in SDSS *r* band, not corrected for the Galactic and internal dust extinction
	Lambda_Re		Specific stellar angular momentum within elliptical half-light isophote, beam corrected[a]
	Sigma_Re	$\mathrm{km\,s^{-1}}$	Effective velocity dispersion within elliptical half-light isophote
	Eps_MGE		Ellipticity of the half-light isophote from MGE fitting
	PA_phot	degree	The photometric position angle (PA[b]) measured from MGE fitting, in SDSS r-band
	PA_kin	degree	The kinematic PA measured from MaNGA velocity field
	PA_kin_flag		The flag for kinematic PA (0 for unreliable, 1 for reliable)
	nsa_iauname		The accepted IAU name
	z		Redshift of the galaxy
	nsa_field		The SDSS field covering the target
	nsa_run		The SDSS run covering the target
	nsa_camcol		The SDSS camcol covering catalogue position
	nsa_version		The version of the NSA catalogue used to select these targets
	nsa_id		The NSAID field in the NSA catalogue v1
	nsa_nsaid_v1b		The NSAID of the target in the NSA_v1b_0_0_v2 catalogue (if applicable)
	nsa_sersic_absmag		Absolute magnitude estimates for FNugriz from K-corrections ($\Omega_{\rm m} = 0.3$, $\Omega_{\Lambda} = 0.7$, $h = 1$), the value is interpreted as $M - 5\lg h$
	nsa_elpetro_absmag		As nsa_sersic_absmag but from elliptical Petrosian apertures
	nsa_sersic_mass	$\lg(\mathrm{h^{-2}\,M_\odot})$	Stellar mass from K-correction fit for Sersic fluxes
	nsa_elpetro_mass	$\lg(\mathrm{h^{-2}\,M_\odot})$	Stellar mass from K-correction fit for elliptical Petrosian fluxes
	nsa_sersic_ba		Axial ratio b/a from 2D Sersic fit in SDSS *r* band
	nsa_sersic_n		Sersic index from 2D Sersic fit in SDSS *r* band
	nsa_sersic_phi	degree	Angle (E of N) of major axis in 2D Sersic fit (*r* band)
	nsa_sersic_th50	arcsec	Sersic 50 per cent light radius along major axis (*r* band)
	nsa_sersic_flux	nanomaggies	2D Sersic fit flux in FNugriz (GALEX-SDSS photometric systems)
	Qual		Visual quality of JAM models, classified as -1, 0, 1, 2, 3 (from worst to best)
	drp3qual		Data reduction quality marked by DRP pipeline, 1 for high-quality, 0 for critical-quality or unusual quality
2	inc_deg	degree	Best-fitting inclination angle (being 90° for edge-on)
($\mathrm{JAM_{cyl}}$+MFL)	beta_z		Best-fitting radial velocity anisotropy in cylindrical coordinates
	log_ML_dyn	$\lg(\mathrm{M_\odot/L_\odot})$	Best-fitting dynamical mass-to-light ratio
	kappa		The ratio between modelled line-of-sight velocity field and the observed one
	log_Mt_Re	$\lg(\mathrm{M_\odot})$	Enclosed total mass within a sphere of effective radius
	chi2_dof		The reduced chi-square of the best-fitting model (The values are scaled to account for the effect of standard deviation of the χ^2 itself, should be only used in the comparison between different models)
	rhalf_arcsec	arcsec	Radius of the sphere which encloses half the total luminosity
	log_Mt_rhalf	$\lg(\mathrm{M_\odot})$	Enclosed total mass within a sphere of 3D half-light radius
	MW_Gt_Re		Mass-weighted total density slope within a sphere of effective radius
	MW_Gt_rhalf		Mass-weighted total density slope within a sphere of 3D half-light radius
	Gt_Re		Average logarithmic total density slope between 0.1 and 1 effective radius

Table B1 – *continued*

HDU (1)	Name (2)	Units (3)	Description (4)
3	inc_deg	degree	Best-fitting inclination angle (being 90° for edge-on)
(JAM_{sph}+MFL)	beta_r		Best-fitting radial velocity anisotropy in spherical coordinates
	log_ML_dyn	$lg(M_\odot/L_\odot)$	Best-fitting dynamical mass-to-light ratio
	kappa		The ratio between modelled line-of-sight velocity field and the observed one
	log_Mt_Re	$lg(M_\odot)$	Enclosed total mass within a sphere of effective radius
	chi2_dof		The reduced chi-square of the best-fitting model (The values are scaled to account for the effect of standard deviation of the χ^2 itself, should be only used in the comparison between different models)
	rhalf_arcsec	arcsec	Radius of the sphere which encloses half the total luminosity
	log_Mt_rhalf	$lg(M_\odot)$	Enclosed total mass within a sphere of 3D half-light radius
	MW_Gt_Re		Mass-weighted total density slope within a sphere of effective radius
	MW_Gt_rhalf		Mass-weighted total density slope within a sphere of 3D half-light radius
	Gt_Re		Average logarithmic total density slope between 0.1 and 1 effective radius
4	inc_deg		Best-fitting inclination angle (being 90° for edge-on)
(JAM_{cyl}+NFW)	beta_z		Best-fitting radial velocity anisotropy in cylindrical coordinates
	log_ML_stellar	$lg(M_\odot/L_\odot)$	Best-fiting stellar mass-to-light ratio
	log_rho_s	$lg(M_\odot\ kpc^{-3})$	The characteristic density of NFW profile
	rs	kpc	The break radius of NFW profile
	kappa		The ratio between modelled line-of-sight velocity field and the observed one
	log_Mt_Re	$lg(M_\odot)$	Enclosed total mass within a sphere of effective radius
	log_Ms_Re	$lg(M_\odot)$	Enclosed stellar mass within a sphere of effective radius
	log_Md_Re	$lg(M_\odot)$	Enclosed DM mass within a sphere of effective radius
	fdm_Re		DM fraction within a sphere of effective radius
	log_ML_dyn_Re	$lg(M_\odot/L_\odot)$	Dynamical mass-to-light ratio within effective radius
	chi2_dof		The reduced chi-square of the best-fitting model (The values are scaled to account for the effect of standard deviation of the χ^2 itself, should be only used in the comparison between different models)
	rhalf_arcsec	arcsec	Radius of the sphere which encloses half the total luminosity
	log_Mt_rhalf	$lg(M_\odot/L_\odot)$	Enclosed total mass within a sphere of 3D half-light radius
	log_Ms_rhalf	$lg(M_\odot/L_\odot)$	Enclosed stellar mass within a sphere of 3D half-light radius
	log_Md_rhalf	$lg(M_\odot/L_\odot)$	Enclosed DM mass within a sphere of 3D half-light radius
	MW_Gt_Re		Mass-weighted total density slope within a sphere of effective radius
	MW_Gs_Re		Mass-weighted stellar density slope within a sphere of effective radius
	MW_Gd_Re		Mass-weighted DM density slope within a sphere of effective radius
	MW_Gt_rhalf		Mass-weighted total density slope within a sphere of 3D half-light radius
	MW_Gs_rhalf		Mass-weighted stellar density slope within a sphere of 3D half-light radius
	MW_Gd_rhalf		Mass-weighted DM density slope within a sphere of 3D half-light radius
	Gt_Re		Average logarithmic total density slope between 0.1 and 1 effective radius
	Gs_Re		Average logarithmic stellar density slope between 0.1 and 1 effective radius
	Gd_Re		Average logarithmic DM density slope between 0.1 and 1 effective radius
5	inc_deg		Best-fitting inclination angle (being 90° for edge-on)
(JAM_{sph}+NFW)	beta_r		Best-fitting radial velocity anisotropy in spherical coordinates
	log_ML_stellar	$lg(M_\odot/L_\odot)$	Best-fitting stellar mass-to-light ratio
	log_rho_s	$lg(M_\odot\ kpc^{-3})$	The characteristic density of NFW profile
	rs	kpc	The break radius of NFW profile
	kappa		The ratio between modelled line-of-sight velocity field and the observed one
	log_Mt_Re	$lg(M_\odot)$	Enclosed total mass within a sphere of effective radius
	log_Ms_Re	$lg(M_\odot)$	Enclosed stellar mass within a sphere of effective radius
	log_Md_Re	$lg(M_\odot)$	Enclosed DM mass within a sphere of effective radius
	fdm_Re		DM fraction within a sphere of effective radius
	log_ML_dyn_Re	$lg(M_\odot/L_\odot)$	Dynamical mass-to-light ratio within effective radius
	chi2_dof		The reduced chi-square of the best-fitting model (The values are scaled to account for the effect of standard deviation of the χ^2 itself, should be only used in the comparison between different models)
	rhalf_arcsec	arcsec	Radius of the sphere which encloses half the total luminosity
	log_Mt_rhalf	$lg(M_\odot/L_\odot)$	Enclosed total mass within a sphere of 3D half-light radius
	log_Ms_rhalf	$lg(M_\odot/L_\odot)$	Enclosed stellar mass within a sphere of 3D half-light radius
	log_Md_rhalf	$lg(M_\odot/L_\odot)$	Enclosed DM mass within a sphere of 3D half-light radius
	MW_Gt_Re		Mass-weighted total density slope within a sphere of effective radius
	MW_Gs_Re		Mass-weighted stellar density slope within a sphere of effective radius
	MW_Gd_Re		Mass-weighted DM density slope within a sphere of effective radius
	MW_Gt_rhalf		Mass-weighted total density slope within a sphere of 3D half-light radius
	MW_Gs_rhalf		Mass-weighted stellar density slope within a sphere of 3D half-light radius
	MW_Gd_rhalf		Mass-weighted DM density slope within a sphere of 3D half-light radius

Table B1 – *continued*

HDU (1)	Name (2)	Units (3)	Description (4)
	Gt_Re		Average logarithmic total density slope between 0.1 and 1 effective radius
	Gs_Re		Average logarithmic stellar density slope between 0.1 and 1 effective radius
	Gd_Re		Average logarithmic DM density slope between 0.1 and 1 effective radius
6	inc_deg		Best-fitting inclination angle (being 90° for edge-on)
(JAM_{cyl}+fixed NFW)	beta_z		Best-fitting radial velocity anisotropy in cylindrical coordinates
	log_ML_stellar	$lg(M_\odot/L_\odot)$	Best-fitting stellar mass-to-light ratio
	log_rho_s	$lg(M_\odot\ kpc^{-3})$	The characteristic density of NFW profile
	rs	kpc	The break radius of NFW profile
	kappa		The ratio between modelled line-of-sight velocity field and the observed one
	log_Mt_Re	$lg(M_\odot)$	Enclosed total mass within a sphere of effective radius
	log_Ms_Re	$lg(M_\odot)$	Enclosed stellar mass within a sphere of effective radius
	log_Md_Re	$lg(M_\odot)$	Enclosed DM mass within a sphere of effective radius
	fdm_Re		DM fraction within a sphere of effective radius
	log_ML_dyn_Re	$lg(M_\odot/L_\odot)$	Dynamical mass-to-light ratio within effective radius
	chi2_dof		The reduced chi-square of the best-fitting model (The values are scaled to account for the effect of standard deviation of the χ^2 itself, should be only used in the comparison between different models)
	rhalf_arcsec	arcsec	Radius of the sphere which encloses half the total luminosity
	log_Mt_rhalf	$lg(M_\odot/L_\odot)$	Enclosed total mass within a sphere of 3D half-light radius
	log_Ms_rhalf	$lg(M_\odot/L_\odot)$	Enclosed stellar mass within a sphere of 3D half-light radius
	log_Md_rhalf	$lg(M_\odot/L_\odot)$	Enclosed DM mass within a sphere of 3D half-light radius
	MW_Gt_Re		Mass-weighted total density slope within a sphere of effective radius
	MW_Gs_Re		Mass-weighted stellar density slope within a sphere of effective radius
	MW_Gd_Re		Mass-weighted DM density slope within a sphere of effective radius
	MW_Gt_rhalf		Mass-weighted total density slope within a sphere of 3D half-light radius
	MW_Gs_rhalf		Mass-weighted stellar density slope within a sphere of 3D half-light radius
	MW_Gd_rhalf		Mass-weighted DM density slope within a sphere of 3D half-light radius
	Gt_Re		Average logarithmic total density slope between 0.1 and 1 effective radius
	Gs_Re		Average logarithmic stellar density slope between 0.1 and 1 effective radius
	Gd_Re		Average logarithmic DM density slope between 0.1 and 1 effective radius
7	inc_deg		Best-fitting inclination angle (being 90° for edge-on)
(JAM_{sph} + fixed NFW)	beta_r		Best-fitting radial velocity anisotropy in spherical coordinates
	log_ML_stellar	$lg(M_\odot/L_\odot)$	Best-fitting stellar mass-to-light ratio
	log_rho_s	$lg(M_\odot\ kpc^{-3})$	The characteristic density of NFW profile
	rs	kpc	The break radius of NFW profile
	kappa		The ratio between modelled line-of-sight velocity field and the observed one
	log_Mt_Re	$lg(M_\odot)$	Enclosed total mass within a sphere of effective radius
	log_Ms_Re	$lg(M_\odot)$	Enclosed stellar mass within a sphere of effective radius
	log_Md_Re	$lg(M_\odot)$	Enclosed DM mass within a sphere of effective radius
	fdm_Re		DM fraction within a sphere of effective radius
	log_ML_dyn_Re	$lg(M_\odot/L_\odot)$	Dynamical mass-to-light ratio within effective radius
	chi2_dof		The reduced chi-square of best-fitting model (The values are scaled to account for the effect of standard deviation of the χ^2 itself, should be only used in the comparison between different models)
	rhalf_arcsec	arcsec	Radius of the sphere which encloses half the total luminosity
	log_Mt_rhalf	$lg(M_\odot/L_\odot)$	Enclosed total mass within a sphere of 3D half-light radius
	log_Ms_rhalf	$lg(M_\odot/L_\odot)$	Enclosed stellar mass within a sphere of 3D half-light radius
	log_Md_rhalf	$lg(M_\odot/L_\odot)$	Enclosed DM mass within a sphere of 3D half-light radius
	MW_Gt_Re		Mass-weighted total density slope within a sphere of effective radius
	MW_Gs_Re		Mass-weighted stellar density slope within a sphere of effective radius
	MW_Gd_Re		Mass-weighted DM density slope within a sphere of effective radius
	MW_Gt_rhalf		Mass-weighted total density slope within a sphere of 3D half-light radius
	MW_Gs_rhalf		Mass-weighted stellar density slope within a sphere of 3D half-light radius
	MW_Gd_rhalf		Mass-weighted DM density slope within a sphere of 3D half-light radius
	Gt_Re		Average logarithmic total density slope between 0.1 and 1 effective radius
	Gs_Re		Average logarithmic stellar density slope between 0.1 and 1 effective radius
	Gd_Re		Average logarithmic DM density slope between 0.1 and 1 effective radius
8	inc_deg		Best-fitting inclination angle (being 90° for edge-on)
(JAM_{cyl}+gNFW)	beta_z		Best-fitting radial velocity anisotropy in cylindrical coordinates
	log_ML_stellar	$lg(M_\odot/L_\odot)$	Best-fitting stellar mass-to-light ratio
	log_rho_s	$lg(M_\odot\ kpc^{-3})$	The characteristic density of gNFW profile
	rs	kpc	The break radius of gNFW profile
	gamma_gNFW		The inner density slope of gNFW profile

Table B1 – *continued*

HDU (1)	Name (2)	Units (3)	Description (4)
	kappa		The ratio between modelled line-of-sight velocity field and the observed one
	log_Mt_Re	lg($M_\odot$)	Enclosed total mass within a sphere of effective radius
	log_Ms_Re	lg($M_\odot$)	Enclosed stellar mass within a sphere of effective radius
	log_Md_Re	lg($M_\odot$)	Enclosed DM mass within a sphere of effective radius
	fdm_Re		DM fraction within a sphere of effective radius
	log_ML_dyn_Re	lg($M_\odot/L_\odot$)	Dynamical mass-to-light ratio within effective radius
	chi2_dof		The reduced chi-square of the best-fitting model (The values are scaled to account for the effect of standard deviation of the χ^2 itself, should be only used in the comparison between different models)
	rhalf_arcsec	arcsec	Radius of the sphere which encloses half the total luminosity
	log_Mt_rhalf	lg($M_\odot/L_\odot$)	Enclosed total mass within a sphere of 3D half-light radius
	log_Ms_rhalf	lg($M_\odot/L_\odot$)	Enclosed stellar mass within a sphere of 3D half-light radius
	log_Md_rhalf	lg($M_\odot/L_\odot$)	Enclosed DM mass within a sphere of 3D half-light radius
	MW_Gt_Re		Mass-weighted total density slope within a sphere of effective radius
	MW_Gs_Re		Mass-weighted stellar density slope within a sphere of effective radius
	MW_Gd_Re		Mass-weighted DM density slope within a sphere of effective radius
	MW_Gt_rhalf		Mass-weighted total density slope within a sphere of 3D half-light radius
	MW_Gs_rhalf		Mass-weighted stellar density slope within a sphere of 3D half-light radius
	MW_Gd_rhalf		Mass-weighted DM density slope within a sphere of 3D half-light radius
	Gt_Re		Average logarithmic total density slope between 0.1 and 1 effective radius
	Gs_Re		Average logarithmic stellar density slope between 0.1 and 1 effective radius
	Gd_Re		Average logarithmic DM density slope between 0.1 and 1 effective radius
9	inc_deg		Best-fitting inclination angle (being 90° for edge-on)
(JAM_{sph}+gNFW)	beta_r		Best-fitting radial velocity anisotropy in spherical coordinates
	log_ML_stellar	lg($M_\odot/L_\odot$)	Best-fitting stellar mass-to-light ratio
	log_rho_s	lg($M_\odot$ kpc^{-3})	The characteristic density of gNFW profile
	rs	kpc	The break radius of gNFW profile
	gamma_gNFW		The inner density slope of gNFW profile
	kappa		The ratio between modelled line-of-sight velocity field and the observed one
	log_Mt_Re	lg($M_\odot$)	Enclosed total mass within a sphere of effective radius
	log_Ms_Re	lg($M_\odot$)	Enclosed stellar mass within a sphere of effective radius
	log_Md_Re	lg($M_\odot$)	Enclosed DM mass within a sphere of effective radius
	fdm_Re		DM fraction within a sphere of effective radius
	log_ML_dyn_Re	lg($M_\odot/L_\odot$)	Dynamical mass-to-light ratio within effective radius
	chi2_dof		The reduced chi-square of the best-fitting model (The values are scaled to account for the effect of standard deviation of the χ^2 itself, should be only used in the comparison between different models)
	rhalf_arcsec	arcsec	Radius of the sphere which encloses half the total luminosity
	log_Mt_rhalf	lg($M_\odot/L_\odot$)	Enclosed total mass within a sphere of 3D half-light radius
	log_Ms_rhalf	lg($M_\odot/L_\odot$)	Enclosed stellar mass within a sphere of 3D half-light radius
	log_Md_rhalf	lg($M_\odot/L_\odot$)	Enclosed DM mass within a sphere of 3D half-light radius
	MW_Gt_Re		Mass-weighted total density slope within a sphere of effective radius
	MW_Gs_Re		Mass-weighted stellar density slope within a sphere of effective radius
	MW_Gd_Re		Mass-weighted DM density slope within a sphere of effective radius
	MW_Gt_rhalf		Mass-weighted total density slope within a sphere of 3D half-light radius
	MW_Gs_rhalf		Mass-weighted stellar density slope within a sphere of 3D half-light radius
	MW_Gd_rhalf		Mass-weighted DM density slope within a sphere of 3D half-light radius
	Gt_Re		Average logarithmic total density slope between 0.1 and 1 effective radius
	Gs_Re		Average logarithmic stellar density slope between 0.1 and 1 effective radius
	Gd_Re		Average logarithmic DM density slope between 0.1 and 1 effective radius

[a]Following equation (5) of Graham et al. (2018).
[b]The standard astronomical PA measured counter-clockwise from the image *Y*-axis (assumed to coincide with North).

This paper has been typeset from a TEX/LATEX file prepared by the author.